“© 2025 IEEE. Personal use of this material is permitted. Permission from IEEE must be obtained for all other uses, in any current or future media, including reprinting/republishing this material for advertising or promotional purposes, creating new collective works, for resale or redistribution to servers or lists, or reuse of any copyrighted component of this work in other works.”

All-Inclusive Image Enhancement for Degraded Images Exhibiting Low-Frequency Corruption

Mingye Ju, *Member, IEEE,* Chunming He, Can Ding, *Senior Member, IEEE,* Wenqi Ren, *Member, IEEE,*
Lin Zhang, *Senior Member, IEEE,* and Kai-Kuang Ma, *Life Fellow, IEEE*

***Abstract*—In this paper, a novel image enhancement method, called the *all-inclusive image enhancement* (AIIE), is proposed that can effectively enhance the degraded images for improving the visibility of image content. These imageries were acquired under various types of weather conditions such as haze, low-light, underwater, and sandstorm, etc. One commonality shared by this class of noise is that the resulted degradations on visual quality or visibility are caused by *low-frequency* interference. Existing image enhancement methods lack the ability to deal with all types of degradations from this class, while our proposed AIIE offers a unified treatment for them. To achieve this goal, a statistical property is obtained from the study of the *discrete cosine transform* (DCT) of 1,000 high- and 1000 low-quality images on their DCT domains. It shows that the normalized DCT coefficients (between 0 and 1) of high-quality images has about 95% fall in the interval [0, 0.2]; for low-quality images, almost all the coefficients are in the same interval. This fundamental property, called the DCT *prior* (DCT-P), is instrumental to the development of our AIIE algorithm proposed in this paper. Since the proposed DCT-P delineates the attributes of high- and low-quality images clearly, it becomes a highly effective tool to convert low-quality images to its enhanced version. Extensive experimental results have clearly validated the superior performance of the AIIE conducted on different types of deteriorated images in terms of visual quality and efficiency as well as significant advantages on computational complexity, which is essential for real-time applications.**

***Index Terms*—All-inclusive image enhancement, discrete cosine transform (DCT), hazy image, underwater image, low-light image.**

I. INTRODUCTION

IMAGES captured under challenging weather conditions, such as hazy, underwater, or low-lighting, often exhibit reduced clarity and lead to poor visibility of the scene, as those deteriorated images demonstrated in Fig. 1. Such acquired images with inferior visual quality can negatively impact the users' experience and hinder the performance of subsequent computer vision tasks [1]. One simple solution to rectify this issue can turn to image enhancement. Techniques like the well-known histogram equalization, for instance, can bolster image contrast by modifying the pixel-value distribution of the acquired image. More advanced techniques, like retinex model-based methods [2], [3], adeptly reveal the intricate details and object contours of obscured scenes. As another set of approaches, gamma correction and homomorphic filter [4], aim to enhance image quality via either the pixel domain or the frequency domain.

While these conventional methods can somewhat ameliorate the quality of degraded images, the resulted image quality improvement is often unsatisfied or inconsistent across various 'noisy' images degraded by different types of weather conditions. For that, a plethora of image enhancement techniques have been devised to handle haze [5]–[17], underwater [18]–[29], and low-lighting [30]–[44]. The strategies involved in the above-mentioned methods predominantly fall into two categories: *prior-based* [5]–[9], [18]–[20], [29]–[34] and *learning-based* [10]–[17], [21]–[28], [35]–[44]. While these approaches have shown encouraging outcomes, the *priors* used in the former category tend to be tailor-made for the chosen type of degradation (say, haze only). For the latter, on the other hand, the training datasets are often established by assembling images arbitrarily chosen from various sources. Such limitations and ad-hoc practice can easily lead to unsatisfied performance for the images acquired in real (unpredictable) weather conditions.

Instead of addressing one specific type of degradation (i.e., specific task), more advanced approaches are developed to handle more than one type of image degradations (i.e., multi-task). Such multi-task image enhancement techniques can be found in neural architecture search [45] and transformers [46]–[56]. However, these approaches often rely on complex networks and synthetic datasets specifically designed for certain types of degradation, leading to long processing time and reduced applicability to real-world environmental conditions. Moreover, they often struggle with addressing the types that have fundamental conflicts on their physical levels. For example, dehazing needs to reduce the brightness, but for the low-light case, brightness is required to be increased.

Our motivation and contributions are derived from the observation that both specific-task and multi-task image enhancement techniques exhibit significant limitations and in-

---

This work was supported by National Natural Science Foundation of China (61902198, 62471253) and Natural Science Foundation of Jiangsu Province (BK20190730), Postdoctoral Science Foundation of China (2021M701728), Research Fund of Nanjing University of Posts and Telecommunications (NY222160), and the general project of natural science research in Colleges and universities of Jiangsu Province (23KJB520027). Mingye Ju and Chunming He contributed equally to this work. (*Corresponding author: Can Ding)*

M. Ju and C. He are with the School of Internet of Things, Nanjing University of Posts and Telecommunications, Nanjing, 210000, China. E-mail:(Jumingye@njupt.edu.cn)

C. Ding is with the Global Big Data Technologies Centre (GBDTC), University of Technology Sydney (UTS), Ultimo, NSW, 2007, Australia. E-mail:(Can.Ding@uts.edu.au)

W. Ren is with the School of Cyber Science and Technology, Sun Yat-sen University, Shenzhen Campus, Shenzhen 518107, China. E-mail:(renwq3@mail.sysu.edu.cn)

L. Zhang is with the School of Software Engineering, Tongji University, Shanghai, 201804, China. E-mail:(cslinzhang@tongji.edu.cn)

K.-K. Ma is with the College of Electronic and Information Engineering, Nanjing University of Aeronautics and Astronautics, Nanjing, 330031, China. E-mail:(kkma23@nuaa.edu.cn)

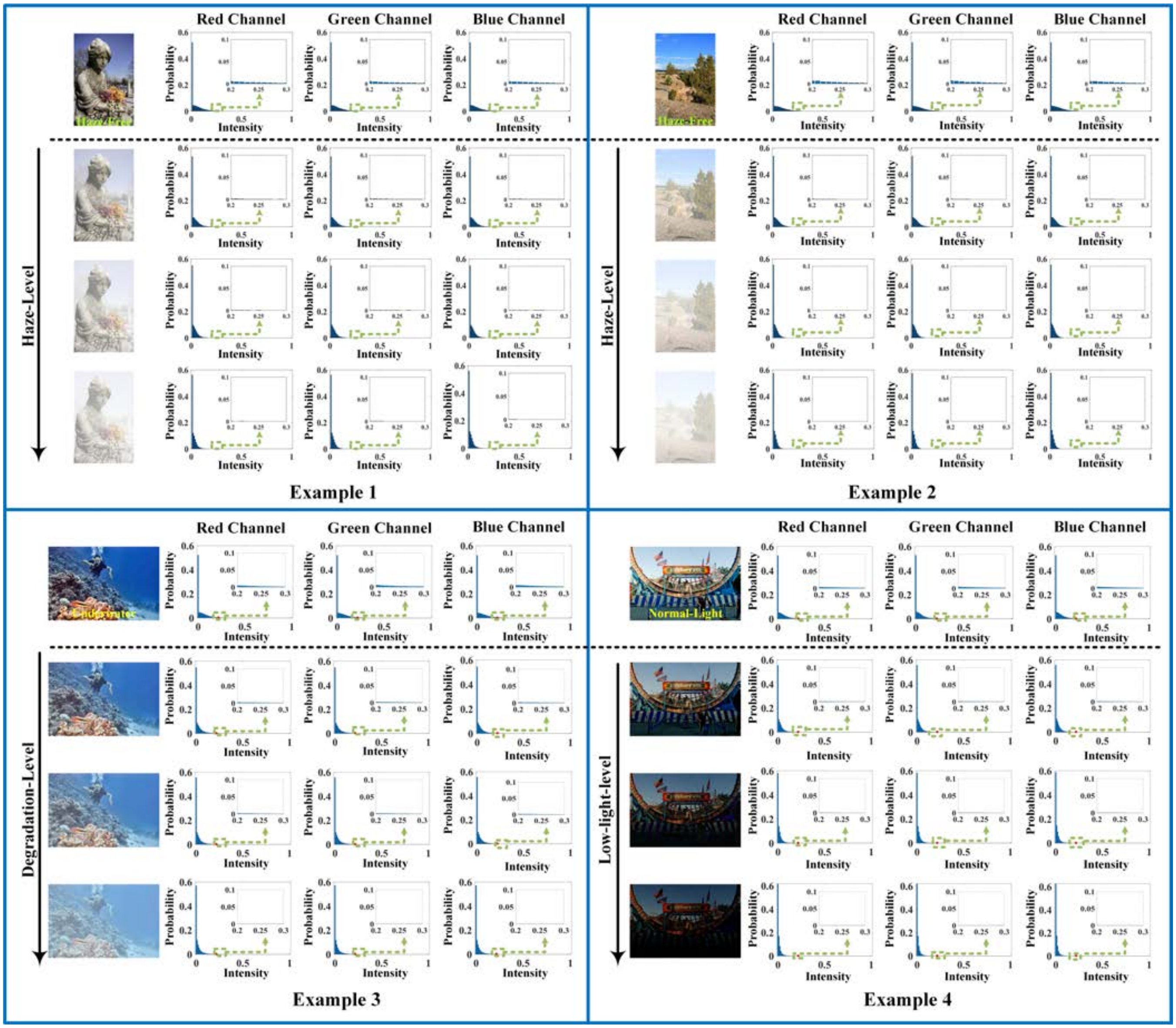

Fig. 1. Examples of low-visibility images and the histogram distributions of their normalized DCT data, between 0 and 1. In each example provided, the first column displays the test images, while the subsequent three columns represent the histogram distributions of DCT data for the R, G, and B channels of these images, respectively.

ternal contradictions (in multi-task cases) in handling various scenarios. Most importantly, none of these approaches are able to provide a unified framework or model to effectively manage images degraded by *low-frequency* corruption, despite the advancements and success accomplished by deep learning and machine intelligence. To provide a fundamental and innovative approach, an all-encompassing image enhancement algorithm based on discrete cosine transform (DCT) [57], called the *all inclusive image enhancement* (AIIE), is proposed in this paper. The core idea of our AIIE is to exploit our discovered *DCT prior* (DCT-P), together with the gray world assumption on the DCT of the degraded image. The heart of AIIE lies in the design of *mask* imposed on the DCT domain, adaptively suppressing low-frequency information while highlighting high-frequency information. Note that the suppressed low-frequency information can effectively remove the interference from the background (i.e., original image content), while the highlighted high-frequency information is able to appropriately enhance the contours and details of the original image content. Such scheme lights up the possibility of recovering those images corrupted by low-frequency interference through such unified treatment.

The main contributions of this paper are summarized as follows:

- To the best of our knowledge, we propose the first image frequency prior, i.e., DCT-P, for those degraded images exhibiting *low*-frequency corruption, such as hazy images, underwater images, and low-light images. The proposed DCT-P is based on the statistics explored on the DCT of high- and low-quality images, showing that about 95% of the normalized DCT coefficient values (between 0 and 1) for a high-quality (i.e., uncorrupted) image lie in the interval of [0, 0.2]; for a low-quality (i.e., corrupted) image, almost all its coefficient values are in this interval. Consequently, this foundational insight enables DCT-P to effectively generalize across a broad spectrum of low-frequency corruption scenarios.

- By leveraging the proposed DCT-P and gray world assumption, a simple but effective image enhancement method, i.e., AIIE is developed. The AIIE grasps the commonality shared by hazy, underwater, and low-lighting, and then employs a mask consisting of two unknown parameters to revise the frequency domain data of degraded images. Unlike currently available related techniques, the proposed algorithm does not require any training process but uses these two priors to gradually determine the unknown parameters, which makes it more robust and efficient.
- Extensive experiments on images and datasets with low-frequency corruption reveal that our proposed AIIE delivers superior performance in visual quality and efficiency compared to leading multi-task approaches. Furthermore, AIIE's results show a considerable advantage over most state-of-the-art methods tailored to individual degradation types.

The remainder of this paper is organized as follows. Following introduction, Section II provides a succinct review of existing relevant works. Section III describes our discovery of the DCT-P and explains why it is a reliable foundation and its derived 'thesis' can be exploited for handling a class of noise that exhibits low-frequency interference to the otherwise high-quality (i.e., clear) image. The model of the proposed AIIE based on DCT-P is developed and presented in Section IV. Section V conducts extensive performance evaluations of our AIIE and existing state-of-the-art approaches. Finally, the conclusions are drawn in Section VI.

II. RELATED WORK

In this section, a brief overview of the research related to specific-task (involving one degradation type) and multi-task (involving multiple degradation types) image enhancement techniques is provided.

A. Specific-Task Image Enhancement

1) Image Dehazing: Early image dehazing techniques [5]–[9] utilized hand-crafted priors to estimate imaging parameters, which were then integrated into the atmospheric scattering model (ASM) for haze removal. The dark channel prior (DCP) [5] was used to estimate the transmission and atmospheric light, which exhibited remarkable effectiveness. Berman et al. [6] introduced a haze-line prior based on recurring color patterns in images. Ju et al. [7] added a light absorption coefficient to the ASM, streamlining dehazing and exposure adjustment, while Agrawal and Jalal [8] used superpixel segmentation to enhance haze removal.

Contrasting to the prior-based approaches, the learning-based techniques [10]–[17] employ deep learning to discern the priors obtained from the hazy and haze-free image pairs. Ren et al. [10] presented a multi-scale CNN dehazing network. Jin et al. [11] combined structure representation with uncertainty feedback for fog removal. EPDN [12], a GAN-based approach, treated dehazing as an image translation problem. RefineDNet [13] combined prior and learning-based techniques, while Zhang et al. [14] provided an attention-based solution by utilizing the Meta-Former framework.

2) Underwater Image Enhancement: Hazy and underwater images tend to share similar visual appearance. Thus, some underwater enhancement algorithms are, in fact, drawn from the dehazing priors or techniques [18]–[20]. For instance, inspired by the DCP for dehazing, Liang et al. [18] modified the DCP for enhancing underwater images. To improve visibility, methods like [19] segment the input image into foreground and background. Ancuti et al. [20] used a white balancing approach to attenuate the red channel for enhancing image naturalness.

With the rise of machine learning, numerous learning-based underwater image enhancement techniques have been introduced [21]–[27]. For instance, a CNN-driven enhancement architecture is presented in [21]. Recognizing that images acquired from the same scene tend to exhibit similar degradations, Qi et al. [22] developed a co-enhancement network using a Siamese encoder-decoder setup. The Retinex-based LAB-MSR [23] was introduced to combat underwater visual distortions, integrating bilateral and trilateral filters to preserve image features. Li et al. [24] offered a lightweight Ucolor network, leveraging features from various color spaces. Additionally, a CNN-centric approach was outlined in [27] to enhance the applicability of machine learning for real world datasets.

3) Low-light Image Enhancement: A range of methods [30]–[34] have been developed to counter the challenges posed by low-light conditions. The LIME method [30] is notable, applying a structure prior to a basic illumination map. Liu et al. [31] proposed a detail-preserving technique for under-exposed images using optimal multi-exposure fusion. Zhang et al. [32] introduced a perception-driven fusion for enhancing under-exposed videos. Techniques based on the Retinex theory have been used to address low illumination issues [33]. A strategy [34] that combined local and global exposedness data was introduced to refine image enhancement quality.

As with the prior techniques, deep learning has been extensively applied to low-light image enhancement [35]–[40]. For example, Lore et al. [35] developed the Low-Light Net (LLNet), which is a deep auto-encoder approach for enhancing visibility and reducing noise. Ren et al. [36] presented a hybrid network, using an encoder-decoder structure, to enhance the visual quality of dim images. A GAN-based system for low-light enhancement, trained through unpaired mappings, was introduced in [37]. Addressing dataset limitations, Peng et al. [38] devised a sliding window approach to generate dynamic training pairs from static videos, leveraging dynamic temporal data to improve low-light images.

B. Multi-Task Image Enhancement

Recently, efforts [45]–[56] have been endeavored on the consideration of designing a universal model for handling multiple types of degradations. Such so-called *multi-task* image enhancement raises the bar of challenges. Notably, existing works like [46]–[48] propose various models such as DualCNN, a residual dense network, and a multi-stage model to cater for different degraded scenarios. However, these require unique datasets for each degradation type to arrive at the training weights that prevent a truly singular network solution for diverse degradation tasks. Li et al. [45] proposed a unified image restoration model, though each encoder must be tailor-made for each degradation type individually. To address these limitations, Valanarasu et al. [49] introduced a single encoder-decoder transformer network for multi-task image enhancement, incorporating a learning module for differentiating weather conditions. Despite its innovation, it struggles with images that have a mixture of degradations.

To explore a viable multi-task restoration strategy, a Blind Image Decomposition Network (BIDeN) [50] featuring one multi-scaled encoder and multiple decoders for each task was proposed. Yet, the necessity to train multiple decoders inevitably adds computational complexity to the model due to the high training cost. Chen et al. [51] pioneered a pre-training approach for multi-task enhancement but encountered challenges in learning shared features due to the model's complexity and specificity requirement. Wang et al. [52] developed a context-aware network aiming at multi-task restoration by leveraging a structure-to-texture enhancement principle. However, it risks semantic distortions in scenes with complex backgrounds [58].

III. PROPOSED DCT PRIOR (DCT-P)

Images of higher visual quality typically exhibit a broader and more evenly distributed histogram. This led us to ponder whether the DCT data of low-quality images due to noise interference would exhibit a similar or a different histogram distribution. To answer this question, the normalized histogram distributions of DCT data for four low-quality images, including two hazy images, one underwater image, and one low-light image, are presented in Fig. 1. Note that, in our work we employ 2D DCT (Type II) to process the entire image, rather than exploiting 8×8 DCT for each 8×8 block non-overlappingly segmented from the image.

Since the DCT coefficients exhibit a near-symmetric Laplacian distribution centered at 0, we truncated negative coefficients to 0 and used Matlab's 'imhist' function for normalization and histogram calculation. The figure clearly illustrates that the DCT data distributions of degraded images differ significantly from their clear counterparts. When the degradation gets severer, the histograms tend to cluster around the origin (i.e., zero value) more. The insets presented in Fig. 1 show a clear trend that while clear images normally have a small fraction of DCT data value > 0.2, the degraded images, on the other hand, predominantly have DCT data < 0.2.

TABLE I
THE AVERAGE VALUES OF $P(\bar{\Psi}^c \leq 0.2)$ ACROSS DIFFERENT TYPES OF DATASETS.

Datasets	I-HAZE			UIEB			LOL		
Color Channels	R	G	B	R	G	B	R	G	B
Ground Truth	0.953	0.947	0.951	0.953	0.952	0.946	0.948	0.956	0.954
Degraded Scenario	0.994	0.989	0.987	0.993	0.995	0.989	0.994	0.993	0.995

Motivated by the observations obtained from Fig. 1, Fig. 2 further displays the histograms and cumulative probability against DCT data value for various types of high-quality and low-quality images, respectively. A fundamental insight can be drawn as follows. For the low-quality images, regardless of their degradation source, almost all DCT data values are < 0.2. In contrast, clear and high-quality images exhibit a small but unneglectable proportion of DCT data values > 0.2. In these cases, the cumulative probabilities are roughly 0.95 for high-quality and 1 for low-quality, respectively. Based on these observations, we introduce a fundamental frequency-domain prior, termed the *DCT prior* (DCT-P):

$$\begin{cases} P(\bar{\Psi}^c \leq 0.2) \approx 0.95, & \text{for high quality images;} \\ P(\bar{\Psi}^c \leq 0.2) \approx 1, & \text{for low quality images.} \end{cases} \tag{1}$$

where $c \in \{\mathrm{R}, \mathrm{G}, \mathrm{B}\}$ is the color index, $\bar{\Psi}^c$ stands for the normalized DCT data of color channel of images.

To validate the accuracy of DCT-P, we conducted tests on 1,000 high-quality images and 1,000 low-quality images. It is important to note that these images were selectively sourced from Google.com[1] using specific tags, such as 'clear natural scenery', 'real bad weather scenery', and 'underwater images'. The outcomes, summarized in Fig. 3, clearly show that the probabilities $P(\bar{\Psi}^c \leq 0.2)$ for high-quality and low-quality images cluster around 0.95 and 1, respectively. In Table I, we further explored the average values of $P(\bar{\Psi}^c \leq 0.2)$ across diverse types of datasets, including haze dataset I-HAZE [59], underwater dataset UIEB [60], and low-light dataset LOL [61]. These results are aligned with those presented in Fig. 3 well, thereby significantly bolstering the credibility of our DCT-P as a highly reliable guide for conducting image enhancement for those low-quality images with degradation. Further tests affirming the impact of DCT-P on image enhancement are detailed in Section V-A.

IV. PROPOSED METHOD: AIIE

Based on the proposed DCT-P discussed in the previous section, a simple yet effective *all-inclusive image enhancement* (AIIE) technique is developed for improving the visibility of various commonly seen low-quality images that they all contribute *low-frequency* interferences. The proposed AIIE consists of two modules—i.e., DCT enhancement modeling module and scene enhancement module.

A. DCT Enhancement Modeling Module

Images captured under challenging weather conditions, such as hazy, underwater, or low-light, often exhibit reduced contrast of the scene and yield poor visibility. In general, the attached background light component mainly affects the low-frequency parts of an image while the vague details are

---

[1] These selected images and the corresponding URL list are available at https://drive.google.com/drive/folders/1wgSoVwx70YLQJzHL6BGazu_4_dEhU_xw?usp=drive_link.

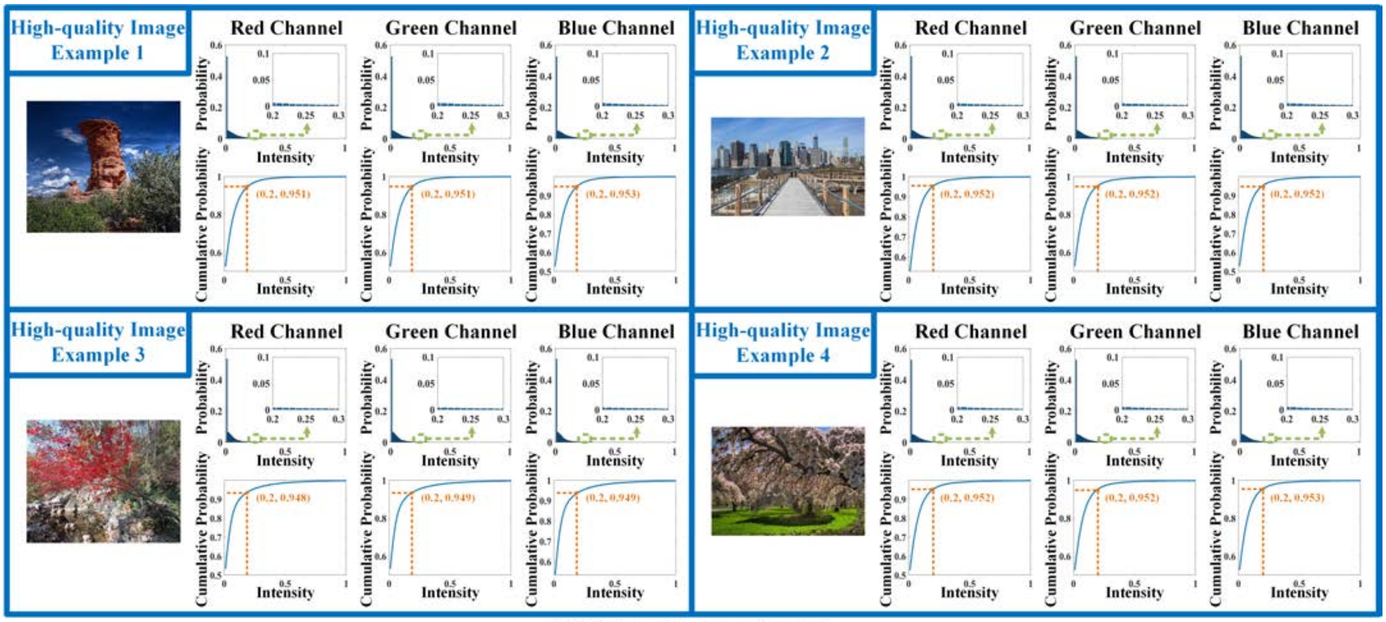

(a) High-quality Image Example

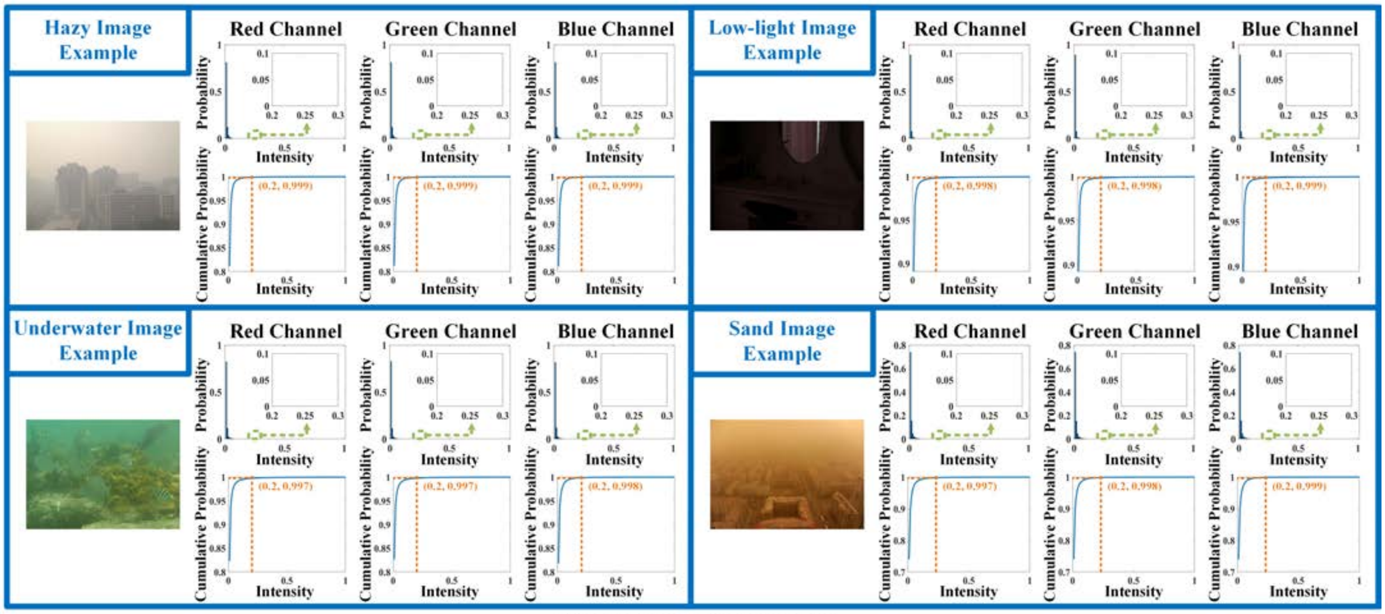

(b) Low-quality Image Example

Fig. 2. The histogram distributions of DCT data and the corresponding cumulative probabilities curves of (a) high-quality and (b) low-quality images. In each example, the upper row details the histogram distributions of DCT data for the test image positioned on the left, followed by the lower row which outlines the cumulative probability curves aligned with the histograms above.

reflected in the weakened high-frequency parts. This means one can enhance such degraded scenes by revising the corresponding frequency domain data. According to this fact, AIIE uses a similar process as the classic homomorphic filtering technique [4] which converts the input image to frequency-domain via Fourier transform, processes the data in frequency-domain by a specific filter or mask, and converts the processed data back to spatial-domain using inverse Fourier transform. In AIIE, the Fourier transform is replaced by DCT and the image enhancement model can be written as

$$R^c = \mathcal{F}^{-1}\Big(\mathcal{F}(I^c) \cdot M^c\Big), \tag{2}$$

where R^c is the enhanced image, I^c is the degraded image, M^c is a mask used to regulate DCT data, $\mathcal{F}(\cdot)$ and $\mathcal{F}^{-1}(\cdot)$ are the DCT operator and inverse DCT operator, respectively.

In our AIIE, the key to achieve high-quality enhancement is to generate a proper mask M^c. Recall in [4], the essence of image enhancement is to suppress its low-frequency information while highlighting the high-frequency information. Meanwhile, it was found that the data closer to the upper left corner in the 2D DCT data domain has a stronger low-frequency attribute [62]. Using this strategy, a flexible mask M^c consisting of two parameters to adjust DCT data is

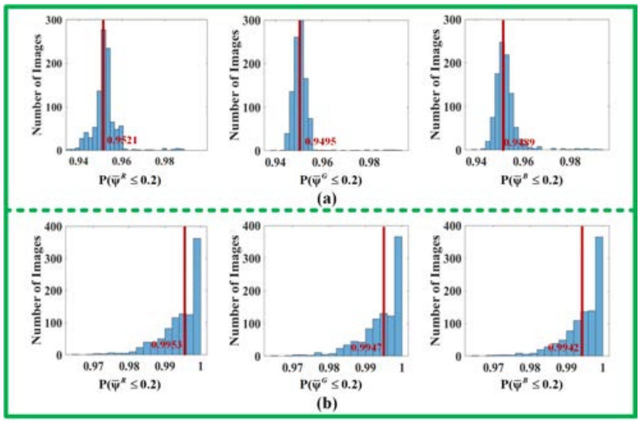

Fig. 3. Distribution of $P(\bar{\Psi}^c \leq 0.2)$ of (a) 1000 high-quality and (b) 1000 low-quality images. As reported, the average values of $P(\bar{\Psi}^c \leq 0.2)$ for high-quality images are concentrated around 0.95, while those for low-quality images are very close to 1.

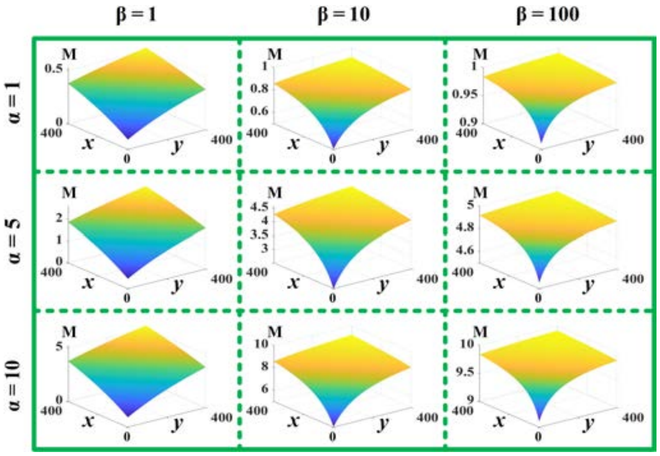

Fig. 4. 2D distribution of M^c with different combinations of α^c and β^c (Note that h and w here are all fixed to be 400 for comparison).

devised:

$$M^c(x,y) = \alpha^c \cdot \left(1 - \frac{1}{1 + \beta^c \cdot \left(\frac{x+y}{h+w} + b\right)}\right), \tag{3}$$

where (x,y) refers to pixel coordinates, h and w stand for the height and width of the degraded image, b is a bias constant used to prevent a too low value of the mask at low-frequency, and α^c and β^c are introduced to control the amplitude and shape of the mask M^c, respectively.

Fig. 4 shows the 2D distribution of M in terms of (x,y) with different combinations of α and β. It is clear that a smaller α leads to a lower amplitude. For example, when $\alpha = 1, \beta = 1$, the maximum amplitude is 0.5; when $\alpha = 10, \beta = 1$, the maximum amplitude is 5. Meanwhile, a larger β slightly lifts up the amplitude and leads to a smaller difference between the amplitudes at low and high frequencies. Furthermore, the value of M increases with x and y, ensuring that low-frequency data are suppressed and high-frequency ones are highlighted.

Substituting Eq. (3) into Eq. (2), the complete DCT image enhancement model can be expressed as

$$\begin{aligned} R^c &= \mathcal{F}^{-1}(F^c_{\alpha,\beta}) = \mathcal{F}^{-1}(F^c \cdot M^c) \\ &= \mathcal{F}^{-1}\left(F^c \cdot \alpha^c \cdot \left(1 - \frac{1}{1 + \beta^c \cdot \left(\frac{x+y}{h+w} + b\right)}\right)\right), \end{aligned} \tag{4}$$

where $\mathcal{F}(I^c)$ in Eq. (2) is written as F^c for short. Thanks to the introduced variables α^c and β^c, the defined model is more malleable than the classic homomorphic filter employing fixed parameters.

When the values of α^c and β^c are appropriately set, high-quality enhancement results can be achieved from degraded images affected by low-frequency corruption, e.g., haze, underwater, and low-light. It is important to note that the devised mask lacks the capability to counteract high-frequency noise corruption. Consequently, the ensuing image enhancement method is not equipped to handle images degraded by rain or snow that exhibit high-frequency corruption.

B. *Scene Enhancement Module*

1) Determining relation between α and β: Gray world assumption (GWA), which assumes that the average albedos of three color channels of an image tend to be the same constant and are achromatic (gray), has been successfully used for color cast correction and haze removal [7]. In this work, GWA is adopted to bridge the relation between α^c and β^c. In specific, we first give the direct current (DC) coefficient of F^c and $F^c_{\alpha,\beta}$ according to [57]:

$$\begin{cases} F^c(1,1) = \dfrac{1}{\sqrt{h \cdot w}} \displaystyle\sum_{x=1}^{h} \sum_{y=1}^{w} I^c(x,y) \\ F^c_{\alpha,\beta}(1,1) = \dfrac{1}{\sqrt{h \cdot w}} \displaystyle\sum_{x=1}^{h} \sum_{y=1}^{w} R^c(x,y). \end{cases} \tag{5}$$

Combining Eq. (5) and Eq. (4) yields

$$F^c_{\alpha,\beta}(1,1) = F^c(1,1) \cdot \alpha^c \cdot \left(1 - \frac{1}{1 + \beta^c \cdot \left(\frac{2}{h+w} + b\right)}\right). \tag{6}$$

Assuming that the enhanced result $\boldsymbol{R}$ is devoid of color cast, i.e., $\boldsymbol{R}$ satisfies the prerequisites of using GWA, the average albedo of R^c can be approximated as

$$G^c = \frac{1}{h \cdot w} \sum_{x=1}^{h} \sum_{y=1}^{w} R^c(x,y) = \frac{F^c_{\alpha,\beta}(1,1)}{\sqrt{h \cdot w}} = 0.5, \tag{7}$$

according to [7]. Substituting Eq. (6) into Eq. (7), the relation between α^c and β^c is finally determined by

$$\begin{aligned} \beta^c &= \Phi(\alpha^c) \\ &= \frac{G^c \cdot \sqrt{h \cdot w}}{\left(F^c(1,1) \cdot \alpha^c - G^c \cdot \sqrt{h \cdot w}\right) \cdot \left(\frac{2}{h+w} + b\right)}, \end{aligned} \tag{8}$$

where $\Phi(\cdot)$ is an abbreviation of Eq. (8).

2) Enhancement using DCT-P: Combining Eqs. (2), (3), and (8), the DCT data after processing can be expressed as a function of α^c:

$$\begin{aligned} F^c_{\alpha,\beta}(x,y) =& \Psi(\alpha^c) \\ =& F^c(x,y)\cdot\alpha^c\cdot\left(1-\frac{1}{1+\Phi(\alpha^c)\cdot\left(\frac{x+y}{h+w}+b\right)}\right), \end{aligned} \tag{9}$$

where $F^c = \mathcal{F}(I^c)$ is the DCT data of the input image, b is the pre-set bias, and α^c is the only unknown parameter. To obtain a suitable value for α^c, a DCT-P based global optimization strategy (GOS) is designed. Mathematically, the GOS is expressed as

$$\alpha^c_p = \arg\min_{\alpha^c}\left\{\left|P(\bar{\Psi}^c(\alpha^c)\le 0.2)-\theta\right|\right\}, \tag{10}$$

where $\bar{\Psi}^c$ is the normalized Ψ^c and θ is set to be 0.95 according to DCT-P. The designed GOS is a 1-D search problem and can be solved via the golden section method (GS). Once α^c_p was computed via GS, the value of β^c and the enhanced results can be directly generated via Eq. (8) and Eq. (4), respectively. The success of designing the above paradigm lies on: 1) The preset mask consisting of two parameters that control the amplitude and shape, i.e., Eq. (3), strictly follows the rule of suppressing the low-frequency component and highlighting the high-frequency component; 2) The relationship between α and β is derived by GWA's interference on DC coefficient, which reduces the uncertainty of calculating mask; 3) By imposing the proposed prior (DCT-P) on the DCT data after processing, the solution space of image enhancement, i.e., the only unknown parameter α is further shrunk and can be solved via the golden section method. The rational design of mask and using two useful priors to gradually approach the actual solution of mask can assure a high-quality image enhancement.

Fig. 5 illustrates the impact of different bias values on the enhancement results and their corresponding masks across various degraded image types. As observed from the figure, a reduced bias yields a more pronounced mask, leading to an intensified suppression of low frequency and a significant amplification of high frequency. This translates to a heightened enhancement effect, giving images richer and more vibrant colors. Nevertheless, this method can lead to noticeable halo effects and over-enhancement in the processed images. Conversely, a higher bias produces a gentler mask, mitigating these unwanted effects but at the expense of the enhancement's vividness. Achieving the ideal balance between enhancing image quality and avoiding such drawbacks proves challenging by directly setting b to a specific value.

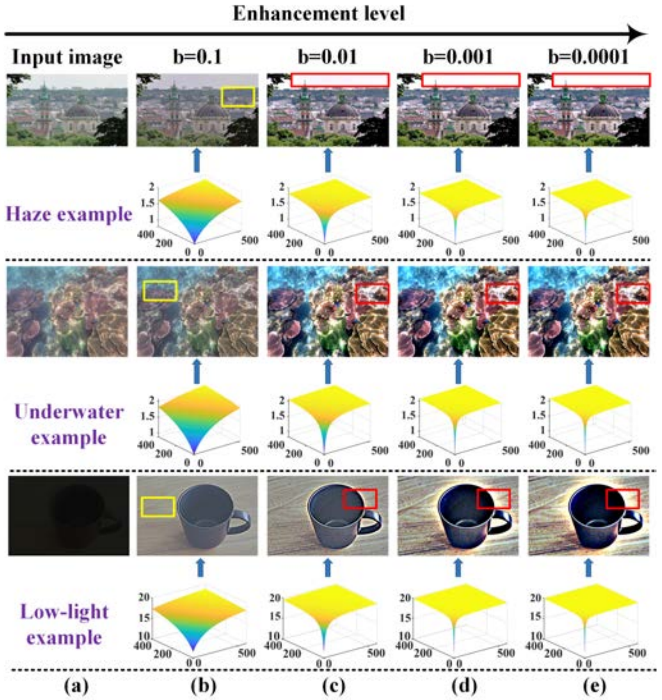

Fig. 5. Performance evaluation across various degraded image types using different biases. For each scenario, the top row showcases the enhanced results, while the bottom row displays the corresponding masks for each bias. (The yellow box is to highlight the insignificant under-enhancement effect while the red box is to illustrate the over-enhancement or over-saturation problem).

3) Iterative enhancement to exclude adverse effects: To tackle the issue previously highlighted, we devised an iterative approach grounded on dynamic bias. The central concept is to incrementally enhance the input image multiple times to achieve optimal results. However, with each iteration, the enhancement is deliberately kept subtle to prevent the halo effect and over-enhancement. Formally, it is described as

$$\begin{cases} R^c_{n+1} =& \mathcal{F}^{-1}\left(\mathcal{F}(R^c_n)\cdot M^c_n\right) \\ M^c_n =& \alpha^c_n\cdot\left(1-\frac{1}{1+\omega\cdot\beta^c_n\cdot\left(\frac{x+y}{h+w}+b_n\right)}\right) \\ b_{n+1} =& b_n/10, \end{cases} \tag{11}$$

where b_n, R^c_n, and M^c_n are the bias, enhanced image, and the corresponding regulation mask of the n^{th} iteration, constant ω is employed to maintain a subtle degree of vagueness in the enhanced results. It is important to note that even on clear days, the atmosphere is not entirely devoid of particles [5], and it is challenging to ensure uniformly abundant lighting for all objects. Thus, preserving a slight vagueness can be beneficial in enhancing the visual realism of the output. In this work, we fix the value of ω to 0.90 for all results reported. The unknown parameters (β^c_n and α^c_n) in M^c_n can be calculated via Eqs. (8) and (10).

The working mechanism behind Eq. (11) can be interpreted as follows: During the initial phase, a larger bias, b, is chosen. This not only curbs the halo effect and over-enhancement but also slightly improves the input image's quality. For the subsequent iteration, the result from the preceding step serves as the new input. Given this improved image (from bias b_n), applying the same bias again yields minimal change. Therefore, to witness a discernible enhancement, a reduced bias (i.e., $b_{n+1} = b_n/10$) is employed. Simultaneously, since the enhancement is subtle, even this smaller b does not

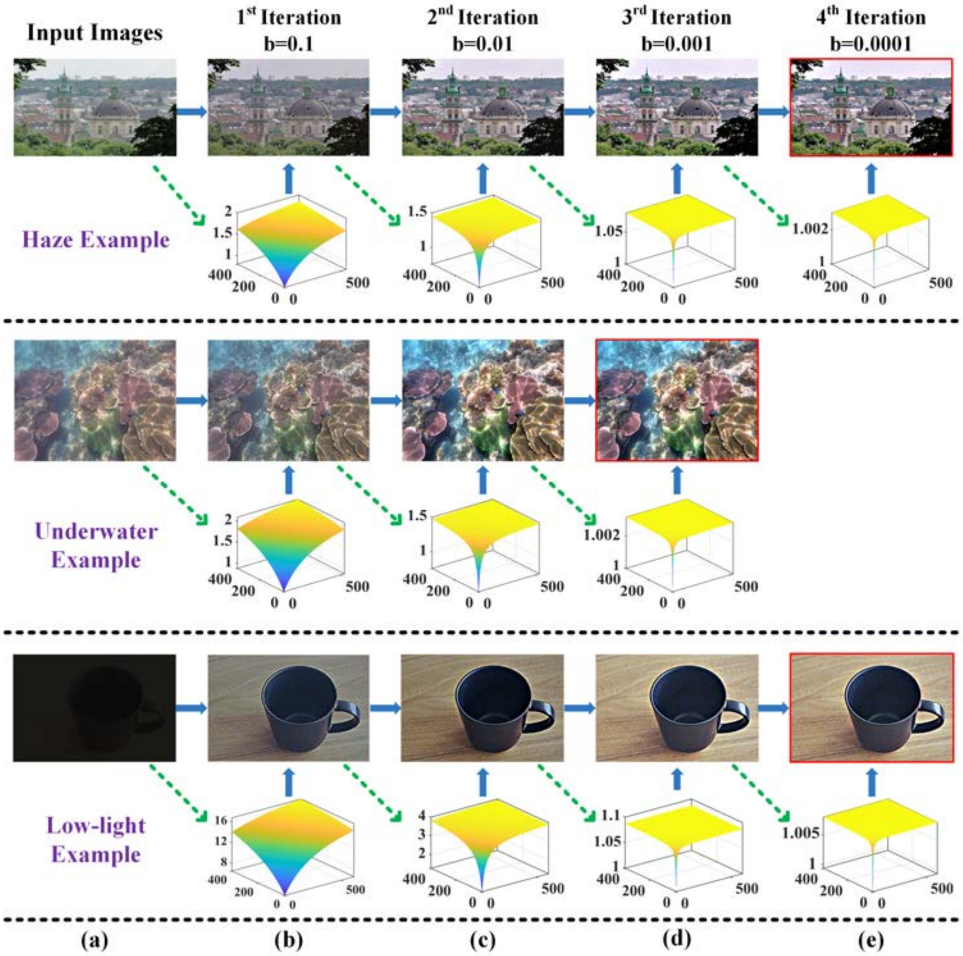

Fig. 6. Illustration of enhancement results achieved by AIIE over different iteration counts. Images framed in red denote the final enhanced outputs, indicating the completion of the iterative process.

induce a halo effect and noise. The process iterates until the image stabilizes. For clearer understanding, the step-by-step procedure of the proposed AIIE is detailed in Algorithm 1.

Fig. 6 displays the enhanced outcomes alongside their corresponding masks generated using AIIE across various iterations. Remarkably, even when employing a notably small value for b, the enhanced images exhibit no discernible halo effect and over-enhancement issue. This consistent clarity can be attributed to the methodical approach of the enhancement: by progressively refining masks without any sudden transitions, the adverse effects are effectively suppressed.

Algorithm 1: Proposed AIIE

```
Input: Degraded image $\boldsymbol{I}$
Initialization:
Iteration times $n = 0$;
Enhanced image $\boldsymbol{R}_0 = \boldsymbol{I}$;
Bias $b_0 = 0.1$ and Parameter $\omega = 0.9$;
while $n == 0$ or $\frac{||\boldsymbol{R}_n - \boldsymbol{R}_{n-1}||_1}{||\boldsymbol{R}_n||_1} < 10^{-3}$ do
    Calculate $\alpha_n^c$ and $\beta_n^c$ from $\boldsymbol{R}_n$ via Eqs. (8) and (10);
    Obtain $\boldsymbol{R}_{n+1}$ and $b_{n+1}$ via Eq. (11);
    $n = n + 1$;
end
Result: Enhanced image $\boldsymbol{R}_n$
```

V. EXPERIMENTS

In this section, a series of experiments were implemented to assess AIIE. First, the effectiveness of DCP-P was evaluated as it is critical to the image enhancement performance. Then the proposed AIIE and traditional image enhancement were tested on different kinds of challenging low-quality images to demonstrate its general applicability. Qualitative and quantitative comparisons were made between AIIE and state-of-the-art technologies, including specific-task image restoration (including image dehazing, underwater image enhancement, and low-light image enhancement methods) and multi-task image enhancement techniques, to exhibit the superiority of AIIE. To ensure fairness and comparability of results, the parameters used in benchmark methods [4], [15], [16], [25], [43], [63]–[66] that require parameter setting were optimized according to the corresponding references, while the remaining methods [11], [17], [24], [26], [27], [40]–[42], [53]–[56] all directly use publicly available trained deep models to test. All experiments were consistently conducted in a standardized environment (an NVIDIA GTX3080Ti GPU and an Intel Core

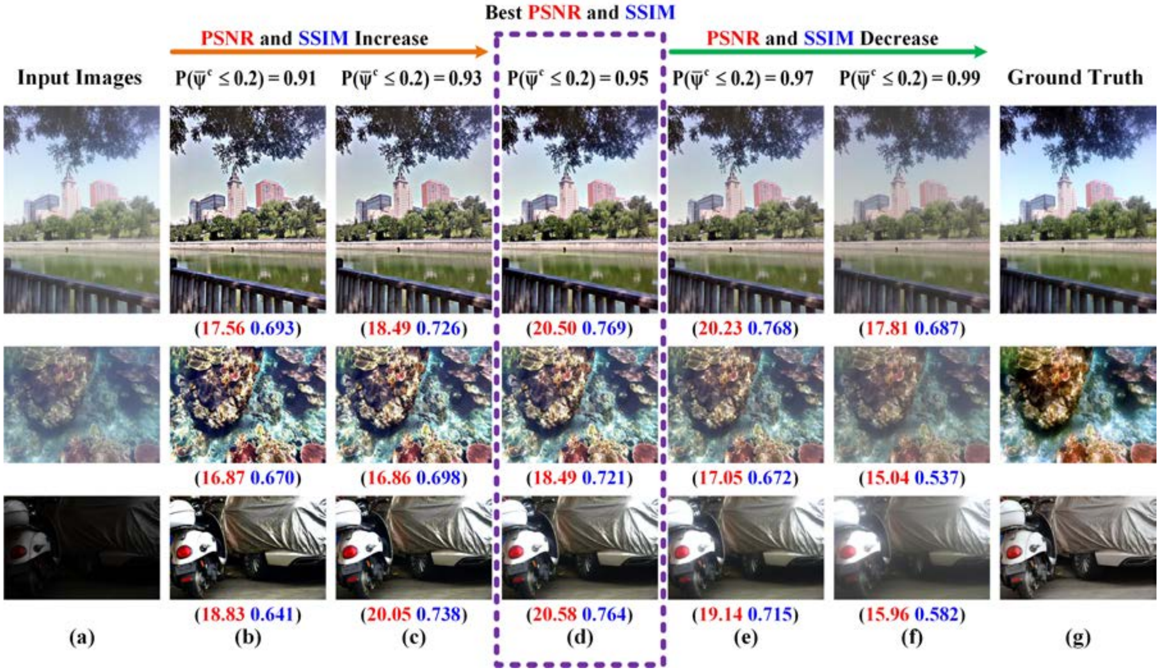

Fig. 7. Image enhancement results using AIIE on different types of degraded images by setting $P(\bar{\Psi}^c \leq 0.2)$ to different values (0.91 to 0.99).

i9-12900H CPU).

A. Evaluation of DCT-P

The effectiveness of DCT-P is the premise to acquiring high-quality recovered results. In Eq. (1), the probability $P(\bar{\Psi}^c \leq 0.2)$ is set to be 0.95 according to the statistics. The accuracy of this value is critical to the performance of AIIE. Three different types of synthesized degraded images collected from datasets [60], [61], [67] together with their ground truth references were tested by the proposed AIIE with different values of $P(\bar{\Psi}^c \leq 0.2)$. During the experiment, peak signal-to-noise ratio (PSNR) and structural similarity index measure (SSIM) [68] were calculated to evaluate the recovered images in quantitative way. Generally, higher PSNR and SSIM represent better fidelity and structure preservation of the recovered results, respectively. The test results are illustrated in Fig. 7. It is observed from the figure that the images are over-enhanced when $P(\bar{\Psi}^c \leq 0.2) < 0.95$, whereas the enhanced results are prone to low-contrast and blur when $P(\bar{\Psi}^c \leq 0.2) > 0.95$. In comparison, $P(\bar{\Psi}^c \leq 0.2) = 0.95$ gives the best results with vivid colors and authentic contrast for all the samples. Moreover, the quantitative results of PSNR and SSIM are consistent with the above qualitative observation, which validates the correctness of DCT-P.

B. Comparison with Traditional Image Enhancement Methods

In this subsection, different categories of degraded images, including low-light images, hazy images, underwater images, sandstorm images, and other types of images with low-frequency corruption, were selected from real-world to make a qualitative comparison between AIIE and traditional image enhancement methods. The low-quality images and the enhanced results using Adaptive Histogram Equalization (AHE) [63], Single Scale Retinex (SSR) [64], Homomorphic Filtering (HF) [4], Gamma Correction (GC) [65], Unsupervised Colour Correction (UCC) [66], and the proposed AIIE are illustrated in Fig. 8.

Fig. 8 showcases the performance of various enhancement methods. While AHE in Fig. 8(b) somewhat improves image visibility, it struggles with scenes affected by color cast, like underwater or sandstorm settings. Fig. 8(c) illustrates that SSR enhances color and contrast, but can not handle over-exposure images well. HF, depicted in Fig. 8(d), addresses contrast for most scenes but can darken results and distort colors. Fig. 8(e) reveals that GC performs well on low-light scenes, yet struggles with other types of low-quality images. UCC, shown in Fig. 8(f), preserves details in underwater and over-exposure scenes while has limitations in other harsh conditions. In contrast, AIIE in Fig. 8(g) consistently delivers visually pleasing results with true colors, sharp details, and high contrast across different scenarios. It is worth mentioning that although AIIE and HF adopt a similar strategy, HF relies on a high-pass filter with two manually adjustable parameters for frequency data manipulation. In contrast, AIIE's parameters are adaptively determined through the application of the DCT probability prior (DCT-P) and the gray world assumption to its mask. This distinction makes AIIE a more stable and practical solution compared to HF. We also compared AIIE quantitatively with traditional methods on synthesized images, yielding consistent results. Given the evident superiority of AIIE in the visual comparison, we have omitted the quantitative data for brevity.

C. Comparison with State-of-The-Art Dehazing Methods

1) Qualitative Comparison: To evaluate the dehazing proficiency of AIIE, five real-world images and five synthesized images from well-known datasets [67], [69] with different haze

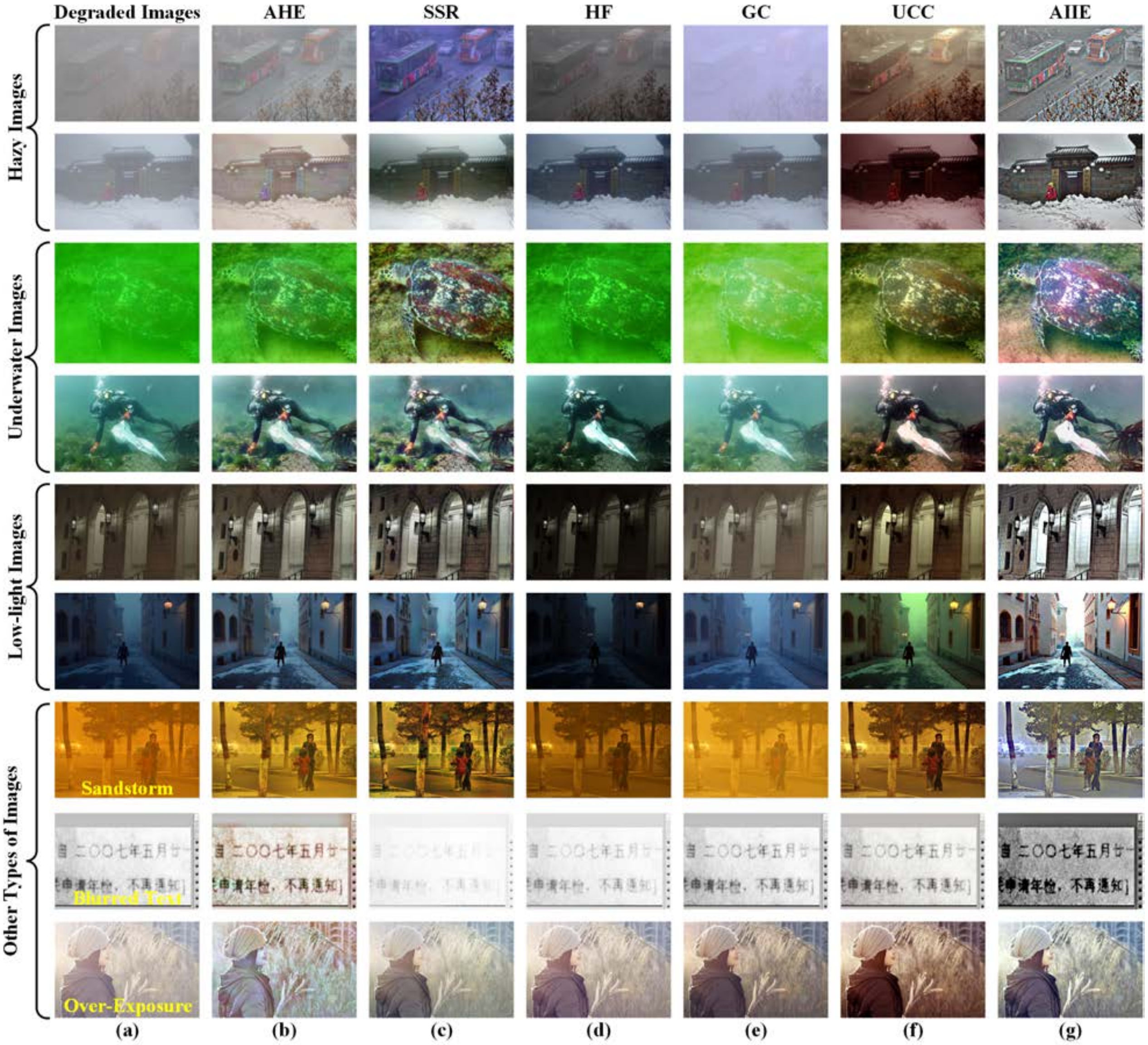

Fig. 8. Qualitative comparison between the proposed AIIE and traditional image enhancement techniques on challenging real-world images.

concentrations were picked and tested. Fig. 9 showcases the dehazing performance comparison between AIIE and leading dehazing approaches such as FR (ACCV 2022) [11], SLP (TIP 2023) [15], SGID-PFF (TIP 2022) [16], and PSD (CVPR 2021) [17].

In Figs. 9(b) and (h), while FR uncovers details obscured by haze, it tends to exhibit over-enhancement (HZP1) and struggles with dense haze scenarios (HZP2). SLP, depicted in Figs. 9(c) and (i), produces generally clear results but sometimes fails to retrieve information from dark areas (HZP3). The SGID-PFF method, shown in Figs. 9(d) and (j), delivers visually appealing images in certain cases but can overcompensate, resulting in lost objects and inaccurate colors (HZP4). PSD, demonstrated in Figs. 9(e) and (k), largely reveals the details for mist images, but its performance tends to be limited for scenes with heavy haze (HZP5). Contrasting these, AIIE's results in Figs. 9(f) and (l) effectively eliminate haze and maintain image fidelity. The enhanced images also retain detailed scene geometry, thanks to the amplified high-frequency information.

2) Quantitative Comparison: The dehazing capability of AIIE was quantitatively evaluated against other leading dehazing methods using four standard metrics: reference metrics PSNR, SSIM, Learned Perceptual Image Patch Similarity (LPIPS) [70], and the non-reference metric Fog Aware Density Evaluator (FADE) [71]. This assessment was conducted on three datasets: I-HAZE [59], O-HAZE [69], and D-HAZE [72]. In addition to quality metrics, we also considered running time (RT) to gauge the efficiency of the dehazing methods. Table II presents the average scores for PSNR, SSIM, LPIPS, FADE, and RT of the various methods. It is important to note that the average PSNR, SSIM, LPIPS, and FADE were computed from the results of AIIE and its competitors across the datasets, while the RT was gauged using the initial 32 images from the D-HAZE dataset. The table reveals that AIIE consistently outperforms or competes closely with top-tier

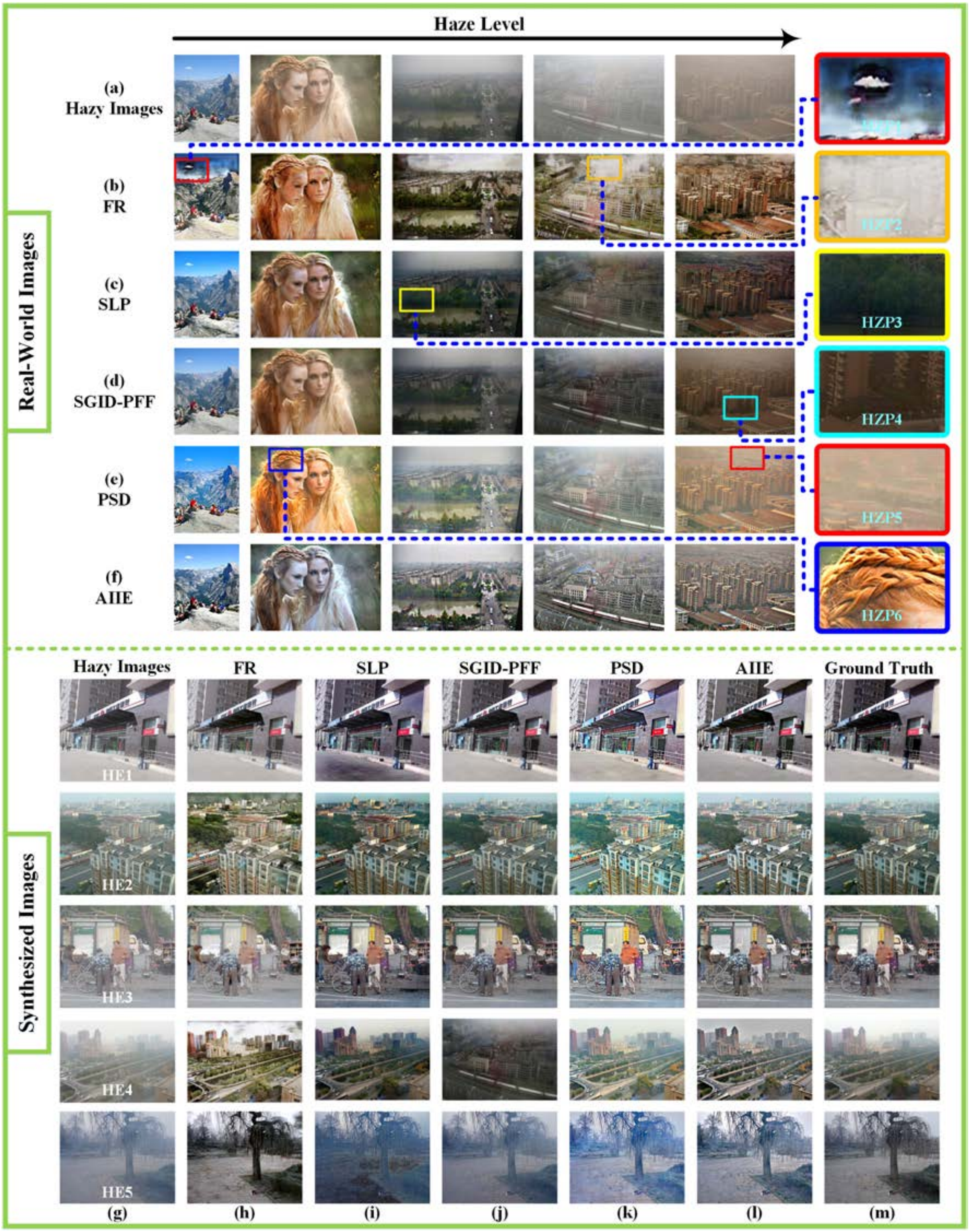

Fig. 9. Qualitative comparison between the proposed AIIE and state-of-the-art dehazing techniques on (a-f) real-world and (g-m) synthetic hazy images.

methods, achieving the second-best FADE scores and leading in RT. For PSNR, SSIM, and LPIPS, AIIE consistently ranks among the top three across the datasets.

D. Comparison with State-of-The-Art Underwater Image Enhancement Methods

1) Qualitative Comparison: To investigate the capability of AIIE to recover underwater images, ten challenging underwater images were selected from both real-world and synthesized datasets [60], [73], [74] to conduct a qualitative comparison between the proposed method and state-of-the-art underwater image enhancement methods, including Ucolor (TIP 2021) [24], ICSP (TCSVT 2023) [25], U-shape (TIP 2023) [26], and SU (AAAI 2021) [27]. The comparative results are showcased in Fig. 10.

In Figs.10(b) and (h), Ucolor efficiently combats the scattering effects in raw underwater images. However, it struggles in scenes with pronounced color casts, evident in (UZP1).

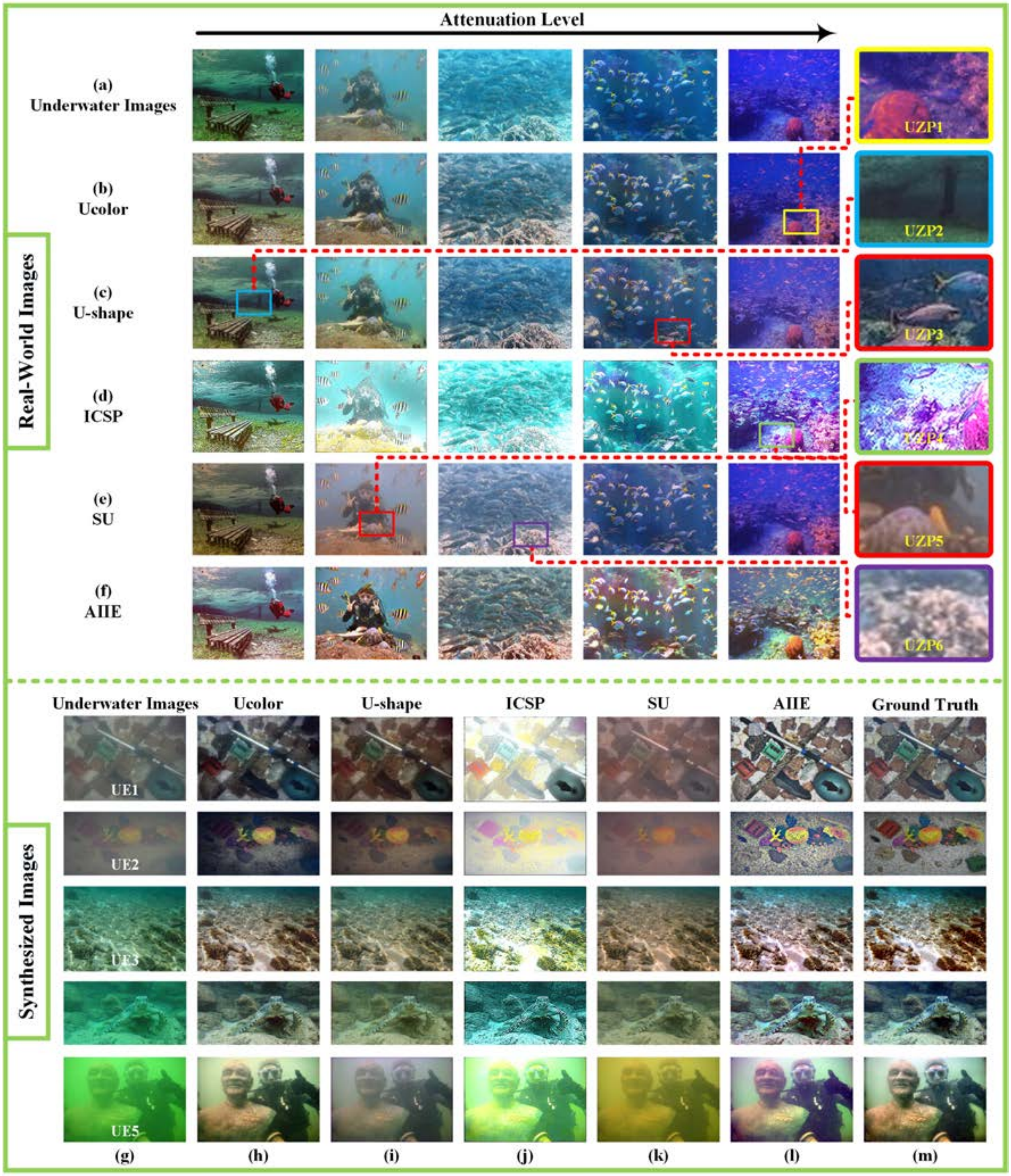

Fig. 10. Qualitative comparison between the proposed AIIE and state-of-the-art underwater image enhancement techniques on challenging (a-f) real-world and (g-m) synthetic underwater images.

Figs.10(c) and (i) showcase U-shape's prowess in unveiling details from mist-obscured underwater scenes, but some of these images appear dim, missing certain details as seen in (UZP2 and UZP3). ICSP, depicted in Figs.10(d) and (j), produces images with acceptable contrast; however, these results may exhibit over-exposure (UZP4) and have color discrepancies. The results from SU, presented in Figs.10(e) and (k), counteract the contrast issues caused by uneven color casts, but sometimes compromise clarity and realism (UZP5 and UZP6). Contrasting these, AIIE, as seen in Figs.10(f) and (l), excels in both detail retrieval and contrast enhancement. The incorporation of GWA in AIIE ensures consistent and natural color representation.

2) Quantitative Comparison: Table III presents the evaluation scores across four metrics: PSNR, SSIM, LPIPS, RT, and the non-reference metric Underwater Image Quality Measures (UIQM) [75]. These metrics are applied across various underwater datasets, including UGAN [73], UIEB [60], and UWCNN [21]. The RT scores are based on the average processing time for the initial 32 images from the UGAN dataset. Notably, AIIE boasts the top UIQM score and is runner-up in RT scores. This underlines AIIE's superior performance in terms of image fidelity and processing speed compared to other leading underwater image enhancement methods. While

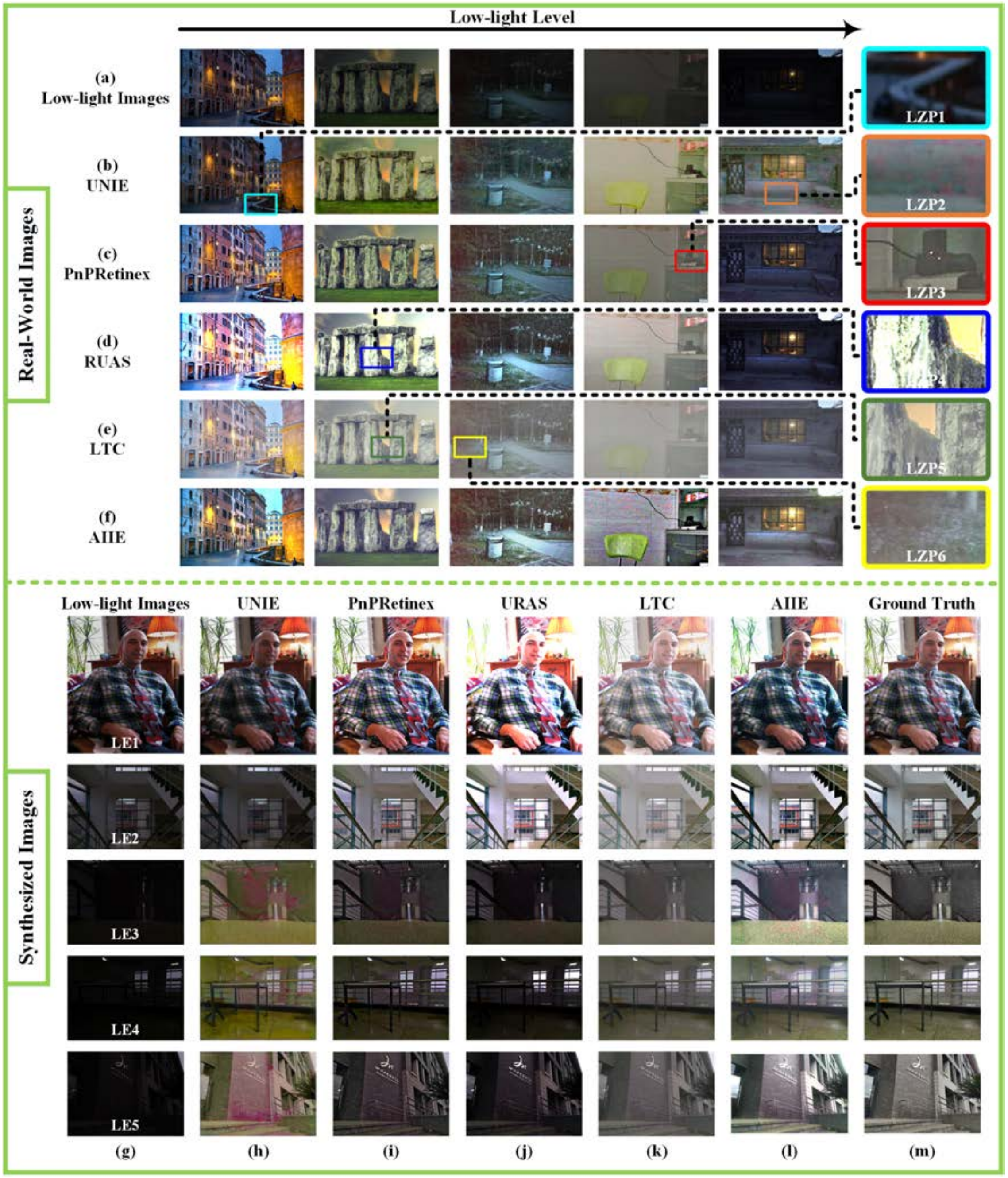

Fig. 11. Qualitative comparison between the proposed AIIE and the state-of-the-art low-light image enhancement techniques on challenging (a-f) real-world and (g-m) synthetic low-light images.

AIIE ranks second or third in PSNR, SSIM, and LPIPS, its enhanced outputs remain on par with other algorithms. The inherent light compensation in AIIE can brighten underwater scenes, leading to disparities between enhanced results and the original image. However, this often results in clearer outputs than the originals, as seen in Fig. 10, making it a beneficial feature rather than a limitation.

E. Comparison with State-of-The-Art Low-Light Image Enhancement Methods

1) Qualitative Comparison: A qualitative assessment pitted AIIE against leading low-light image enhancement methods, including UNIE (ECCV 2022) [41], RUAS (TPAMI 2022) [42], PnPRetinex (TIP 2022) [43], and LTC (CVPR 2021) [40]. Ten low-light images, sourced from both real-world scenarios and dataset [44], served as test subjects, with results displayed in Fig. 11.

In Figs.11(b) and (h), while UNIE compensates for dark regions and highlights details, certain textured regions (LZP1 and LZP2) appear to lose necessary information. Figs.11(c) and (i) show PnPRetinex's ability to revive scene details and reconstruct illumination, but some regions appear blurred, compromising visibility (LZP3). RUAS, seen in Figs.11(d) and (j), adeptly reconstructs image brightness, yet the re-

TABLE II
Quantitative comparison between AIIE and dehazing methods on different datasets. (Data highlighted in bold represents the best performance, while data in blue signifies the second-best.)

Methods (Platform)	Datasets	PSNR↑	SSIM↑	LPIPS↓	FADE↓	RT↓(s)
FR Pytorch(GPU)	I-HAZE	15.91	0.560	0.221	**0.368**	0.152
	O-HAZE	**18.37**	**0.660**	0.266	**0.280**	
	D-HAZE	11.77	0.565	0.506	0.582	
SLP Matlab(CPU)	I-HAZE	14.95	0.690	0.120	0.503	0.213
	O-HAZE	16.19	0.622	0.209	0.336	
	D-HAZE	14.49	**0.757**	**0.091**	**0.406**	
SGID-PFF Pytorch(GPU)	I-HAZE	15.67	0.706	0.174	0.936	0.083
	O-HAZE	16.44	0.596	0.245	0.804	
	D-HAZE	10.14	0.640	0.151	0.888	
PSD Pytorch(GPU)	I-HAZE	13.54	0.583	**0.116**	0.991	0.390
	O-HAZE	11.44	0.350	0.199	0.481	
	D-HAZE	10.53	0.625	0.162	0.859	
AIIE Matlab(CPU)	I-HAZE	**16.13**	**0.710**	0.151	0.507	**0.077**
	O-HAZE	17.11	0.637	**0.192**	0.295	
	D-HAZE	**14.91**	0.647	0.154	0.469	

TABLE IV
Quantitative comparison between AIIE and low-light image enhancement methods. (Data highlighted in bold represents the best performance, while data in blue signifies the second-best.)

Methods (Platform)	Datasets	PSNR↑	SSIM↑	LPIPS↓	CEIQ↑	RT↓(s)
PnPRetinex Matlab(CPU)	SYD	13.99	0.605	**0.123**	2.909	5.166
	LOL	12.38	0.477	0.156	2.705	
	GLAD	17.28	**0.798**	**0.083**	3.010	
RUAS Pytorch(GPU)	SYD	14.12	0.531	0.186	2.994	0.101
	LOL	12.16	0.501	0.155	2.745	
	GLAD	13.35	0.637	0.181	3.283	
LTC Pytorch(GPU)	SYD	**20.74**	**0.873**	0.134	3.295	0.073
	LOL	17.34	0.749	0.169	2.677	
	GLAD	16.40	0.721	0.115	3.076	
UNIE Pytorch(GPU)	SYD	12.60	0.544	0.293	2.831	0.148
	LOL	**23.76**	**0.856**	**0.118**	3.187	
	GLAD	14.83	0.607	0.194	2.985	
AIIE Matlab(CPU)	SYD	17.38	0.663	0.132	**3.407**	**0.061**
	LOL	18.95	0.767	0.163	**3.534**	
	GLAD	**18.05**	0.730	0.136	**3.561**	

TABLE III
Quantitative comparison between AIIE and underwater image enhancement methods. (Data highlighted in bold represents the best performance, while data in blue signifies the second-best.)

Methods (Platform)	Datasets	PSNR↑	SSIM↑	LPIPS↓	UIQM↑	RT↓(s)
SU TensorFlow(GPU)	UGAN	15.76	0.736	0.117	0.638	0.103
	UIEB	16.25	0.671	0.228	0.468	
	UWCNN	13.88	0.530	0.293	0.170	
U-shape Pytorch(GPU)	UGAN	**19.94**	**0.783**	**0.115**	0.593	**0.024**
	UIEB	**21.87**	**0.822**	0.098	0.634	
	UWCNN	12.23	0.592	0.226	0.574	
Ucolor TensorFlow(GPU)	UGAN	18.94	0.573	0.138	0.649	29.470
	UIEB	21.38	0.816	**0.077**	0.770	
	UWCNN	**19.69**	**0.672**	**0.103**	0.358	
ICSP Matlab(CPU)	UGAN	11.61	0.467	0.327	0.918	0.083
	UIEB	10.55	0.522	0.398	0.979	
	UWCNN	9.39	0.476	0.311	0.559	
AIIE Matlab(CPU)	UGAN	16.97	0.631	0.125	**1.072**	0.073
	UIEB	21.55	0.778	0.119	**1.040**	
	UWCNN	18.99	0.613	0.151	**1.208**	

sulting images have blurred textures (LZP4). LTC, displayed in Figs.11(e) and (k), enhances global exposure, but details appear blurred (LZP5 and LZP6). In contrast, AIIE, as shown in Figs.11(f) and (l), effectively compensates for lighting, avoiding pitfalls like unrealistic textures or pronounced noise.

2) Quantitative Comparison: In a more in-depth evaluation of AIIE's performance on low-light images, we conducted a quantitative analysis against leading methods, using metrics such as PSNR, SSIM, LPIPS, RT, and the no-reference metric contrast-enhanced image quality (CEIQ) [76]. Results from the SYD [44], LOL [61], and GLAD [77] datasets are summarized in Table IV. It is noteworthy that the RT value was determined using the first 32 images from SYD. The table indicates AIIE's superior performance, achieving the top CEIQ and the best RT across all datasets. In terms of PSNR, SSIM, and LPIPS, AIIE consistently ranks within the top three for all datasets.

F. Comparison with State-of-The-Art Multi-Task Image Enhancement Methods

1) Qualitative Comparison: Fig. 12 showcases the visual comparison of AIIE against leading multi-task image enhancement techniques, including AirNet (CVPR 2022) [53], AOSR (ICTAI 2023) [54], TSK (CVPR 2022) [55], and DA-CLIP (ICLR 2024) [56]. Four categories of degraded imageslow-light, sandstorm, haze, and underwater conditionswere chosen from both real-world sources and specific datasets, including LOL, O-HAZE, and UIEB. Notably, the sandstorm dataset (O-SS) was synthesized from O-HAZE using Adobe Photoshop. In Figs. 12(b) and (h), AirNet marginally improves image quality but struggles with scenes featuring dense haze or low lighting (MZP1 and MZP2). The AOSR approach, depicted in Figs. 12(c) and (i), delivers aesthetically pleasing results in certain scenarios, yet tends to darken the background brightness in underwater images (MZP3). TSK, effective in refining underwater and hazy images, shows limitations for low-light conditions as demonstrated in Figs. 12(d) and (j) (MZP4). DA-CLIP, shown in Figs. 12(e) and (k), excels in enhancing low-light images but falls short in addressing sandstorm and haze (MZP5 and MZP6). Observations from Figs. 12(f) and (l) reveal that AIIE successfully mitigates adverse effects in hazy, underwater, low-light, and sandstorm images, surpassing the performance of other multi-task solutions.

2) Quantitative Comparison: Table V ranks the performance of various multi-task image enhancement methods across four distinct dataset types, with metrics scores reported for each. The RT scores reflect the average processing time for the first 32 images from the O-SS dataset. As shown, AIIE secures the top position on O-HAZE, UNIE, and O-SS datasets, and places as the runner-up on the LOL dataset, outperforming in both reference and non-reference metrics, notably in efficiency compared to the other methods. Given that DA-CLIP was trained on the LOL dataset, it is expected that AIIE may not outscore DA-CLIP in this context. However,

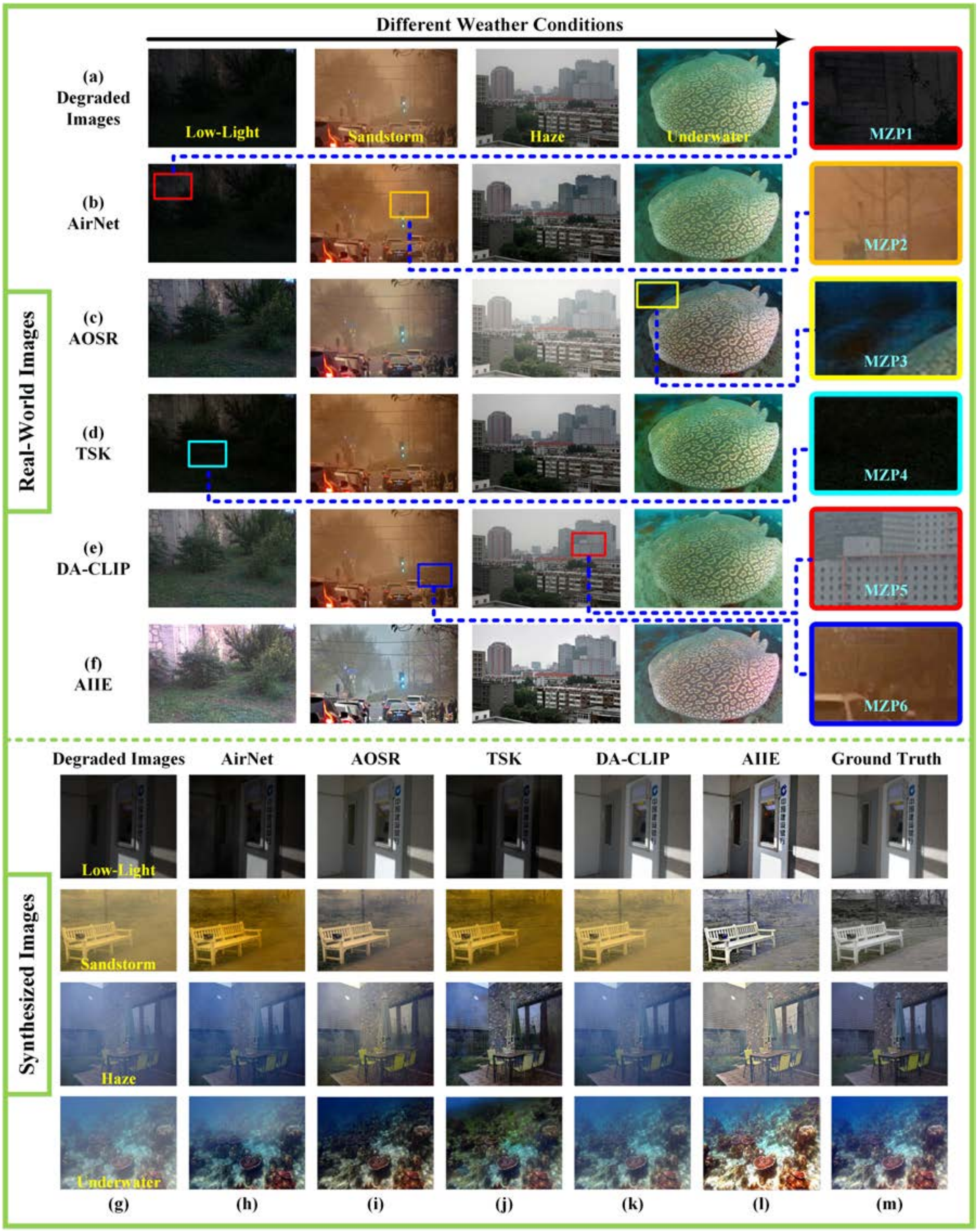

Fig. 12. Qualitative comparison between the proposed AIIE and state-of-the-art multi-task image enhancement techniques on (a-f) real-world and (h-m) synthetic degraded images.

AIIE demonstrates superior generalization in handling real-world images, as evident in Fig.12. More importantly, the processing time of our AIIE (0.066s) is significantly shorter than that of DA-CLIP (8.615s), which ensures the real-time performance of AIIE.

Overall, regardless of whether the images are hazy, underwater, sandstorm, or taken in low-light conditions, our proposed AIIE consistently delivers satisfactory enhancement results in a timely manner. The effectiveness of AIIE is attributed to its ability to operate without a training process and without the need to discern the specific degradation of the image. Instead, it effectively taps into the frequency domain characteristics, suppressing low-frequency details while accentuating high-frequency elements. As such, AIIE emerges as a robust solution for enhancing degraded images with low-frequency corruption.

TABLE V

QUANTITATIVE COMPARISON BETWEEN AIIE AND MULTI-TASK IMAGE ENHANCEMENT METHODS ON DIFFERENT DATASETS. (DATA HIGHLIGHTED IN BOLD REPRESENTS THE BEST PERFORMANCE, WHILE DATA IN BLUE SIGNIFIES THE SECOND-BEST.)

Dataset	Metric	AirNet	AoSRNet	TSK	DA-CLIP	AIIE
O-HAZE	PSNR↑	15.46	15.03	16.96	15.74	**17.11**
	SSIM↑	0.412	0.600	0.629	0.579	**0.637**
	LPIPS↓	0.248	0.196	0.203	0.367	**0.192**
	FADE↓	0.840	0.917	0.339	0.804	**0.295**
UIEB	PSNR↑	15.41	15.32	15.61	17.33	**21.55**
	SSIM↑	0.6710	0.764	0.710	0.698	**0.778**
	LPIPS↓	0.157	0.126	0.162	0.277	**0.119**
	UIQM↑	0.396	0.768	0.501	0.441	**1.040**
LOL	PSNR↑	7.44	12.81	8.03	**29.21**	18.95
	SSIM↑	0.131	0.527	0.230	**0.846**	0.767
	LPIPS↓	0.394	0.168	0.391	**0.083**	0.163
	CEIQ↑	1.733	2.779	1.937	3.243	**3.534**
O-SS	PSNR↑	12.56	16.31	14.89	14.31	**18.67**
	SSIM↑	0.527	0.627	0.542	0.658	**0.762**
	LPIPS↓	0.192	0.171	0.236	0.239	**0.125**
	NIQE↓	7.621	6.621	7.760	7.493	**5.919**
	RT↓(s)	0.411	0.134	0.116	8.615	**0.066**

G. Limitation

Note that the proposed AIIE method is developed to deal with degraded images exhibiting low-frequency corruption (as highlighted in the papers title), thus, as expected, AIIE may not be able to completely remove the noise on the images containing high-frequency corruption. To clarify this, a comparison between the multi-task image enhancement techniques and our AIIE is further illustrated in Figs. 13. As shown, both the multi-task image enhancement techniques and our proposed AIIE are unable to completely remove the raindrops in such a heavy rain situation. Nonetheless, this is still highly welcome and useful, since it improves the visibility of the scene (e.g., see the red-framed region). Note that AIIE have delivered the best clarity compared to those of other approaches. This is due to the fact that the light/misty raindrops, sharing the same low-frequency corruption properties as haze or fog, have been effectively reduced.

VI. CONCLUSION

According to our extensive studies, several commonly encountered types of weather-affected image degradations, such as haze, fog, low light, underwater, sandstorm, and so on, all exhibit *low-frequency* interference or corruption. This fundamental discovery motivated us to develop a *single* solution to tackle *all* types of degradations resulted from this class of noise. A high majority of existing image enhancement techniques can only handle one specific type of degradation (i.e., specific-task), and only few address two or more types (i.e., multi-task), to our best knowledge. In contrast, our proposed *all-inclusive image enhancement* (AIIE) is able to handle all types of degradations from this class! The commonality of this 'low-frequency corruption' motivates us to consider a DCT-domain approach. First, a fundamental statistical property is explored in the normalized DCT coefficient data field that leads to our DCT prior (DCT-P). The key success of our proposed AIIE lies in the development of image *enhancement mask* involving two adaptive parameters and their values are iteratively determined based on the DCT-P and the gray-world assumption.

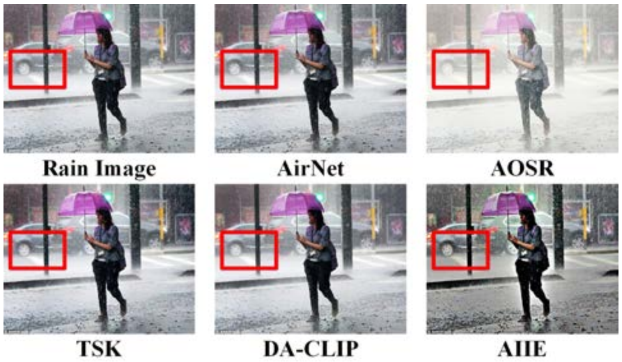

Fig. 13. An example illustration of a rain image to showcase the limitation of the proposed AIIE.

Extensive experimental results have clearly shown the superior image enhancement performance achieved by our AIIE against most state-of-the-art methods in both specific-task or multi-task scenarios. Besides the *efficiency*, our AIIE is also advantageous on *efficacy*, from the viewpoints of computational complexity and algorithmic complexity. Indeed, the computation time of AIIE is significantly faster than that of state-of-the-arts, mainly due to our AIIE is a signal processing approach without involving computational-intensive machine learning approach and related dataset issues. All these are critical for those image-based applications, such as unmanned auto-driving vehicles, drones, and so on, in which real-time performance is often required.

REFERENCES

[1] M. Shakeri and H. Zhang, "Moving object detection in time-lapse or motion trigger image sequences using low-rank and invariant sparse decomposition," in *2017 IEEE International Conference on Computer Vision (ICCV)*, 2017, pp. 5133–5141.

[2] Z. Rahman, D. Jobson, and G. Woodell, "Multi-scale retinex for color image enhancement," in *Proceedings of 3rd IEEE International Conference on Image Processing*, vol. 3, 1996, pp. 1003–1006 vol.3.

[3] G. Guarnieri, S. Marsi, and G. Ramponi, "High dynamic range image display with halo and clipping prevention," *IEEE Transactions on Image Processing*, vol. 20, no. 5, pp. 1351–1362, 2011.

[4] A. Oppenheim, R. Schafer, and T. Stockham, "Nonlinear filtering of multiplied and convolved signals," *Proceedings of the IEEE*, vol. 56, no. 8, pp. 1264–1291, 1968.

[5] K. He, J. Sun, and X. Tang, "Single image haze removal using dark channel prior," *IEEE Transactions on Pattern Analysis and Machine Intelligence*, vol. 33, no. 12, pp. 2341–2353, 2011.

[6] D. Berman, T. Treibitz, and S. Avidan, "Single image dehazing using haze-lines," *IEEE Transactions on Pattern Analysis and Machine Intelligence*, vol. 42, no. 3, pp. 720–734, 2020.

[7] M. Ju, C. Ding, W. Ren, Y. Yang, D. Zhang, and Y. J. Guo, "Ide: Image dehazing and exposure using an enhanced atmospheric scattering model," *IEEE Transactions on Image Processing*, vol. 30, pp. 2180–2192, 2021.

[8] S. C. Agrawal and A. S. Jalal, "Dense haze removal by nonlinear transformation," *IEEE Transactions on Circuits and Systems for Video Technology*, vol. 32, no. 2, pp. 593–607, 2022.

[9] S. Kanti Dhara, M. Roy, D. Sen, and P. Kumar Biswas, "Color cast dependent image dehazing via adaptive airlight refinement and non-linear color balancing," *IEEE Transactions on Circuits and Systems for Video Technology*, vol. 31, no. 5, pp. 2076–2081, 2021.

[10] W. Ren, S. Liu, H. Zhang, J. Pan, X. Cao, and M.-H. Yang, "Single image dehazing via multi-scale convolutional neural networks," in *Computer Vision – ECCV 2016*, B. Leibe, J. Matas, N. Sebe, and M. Welling, Eds. Cham: Springer International Publishing, 2016, pp. 154–169.

[11] Y. Jin, W. Yan, W. Yang, and R. T. Tan, "Structure representation network and uncertainty feedback learning for dense non-uniform fog removal," in *Asian Conference on Computer Vision*. Springer, 2022, pp. 155–172.

[12] Y. Qu, Y. Chen, J. Huang, and Y. Xie, "Enhanced pix2pix dehazing network," in *2019 IEEE/CVF Conference on Computer Vision and Pattern Recognition (CVPR)*, 2019, pp. 8152–8160.

[13] S. Zhao, L. Zhang, Y. Shen, and Y. Zhou, "Refinednet: A weakly supervised refinement framework for single image dehazing," *IEEE Transactions on Image Processing*, vol. 30, pp. 3391–3404, 2021.

[14] G. Zhang, W. Fang, Y. Zheng, and R. Wang, "Sdbad-net: A spatial dual-branch attention dehazing network based on meta-former paradigm," *IEEE Transactions on Circuits and Systems for Video Technology*, pp. 1–1, Early Access, 2023, doi: 10.1109/TCSVT.2023.3274366.

[15] P. Ling, H. Chen, X. Tan, Y. Jin, and E. Chen, "Single image dehazing using saturation line prior," *IEEE Transactions on Image Processing*, vol. 32, pp. 3238–3253, 2023.

[16] H. Bai, J. Pan, X. Xiang, and J. Tang, "Self-guided image dehazing using progressive feature fusion," *IEEE Transactions on Image Processing*, vol. 31, pp. 1217 – 1229, 2022.

[17] Z. Chen, Y. Wang, Y. Yang, and D. Liu, "Psd: Principled synthetic-to-real dehazing guided by physical priors," in *Proceedings of the IEEE/CVF Conference on Computer Vision and Pattern Recognition (CVPR)*, June 2021, pp. 7180–7189.

[18] Z. Liang, X. Ding, Y. Wang, X. Yan, and X. Fu, "Gudcp: Generalization of underwater dark channel prior for underwater image restoration," *IEEE Transactions on Circuits and Systems for Video Technology*, vol. 32, no. 7, pp. 4879–4884, 2022.

[19] J. Y. Chiang and Y.-C. Chen, "Underwater image enhancement by wavelength compensation and dehazing," *IEEE Transactions on Image Processing*, vol. 21, no. 4, pp. 1756–1769, 2012.

[20] C. O. Ancuti, C. Ancuti, C. De Vleeschouwer, and P. Bekaert, "Color balance and fusion for underwater image enhancement," *IEEE Transactions on Image Processing*, vol. 27, no. 1, pp. 379–393, 2018.

[21] C. Li, S. Anwar, and F. Porikli, "Underwater scene prior inspired deep underwater image and video enhancement," *Pattern Recognition*, vol. 98, p. 107038, 2020.

[22] Q. Qi, Y. Zhang, F. Tian, Q. M. J. Wu, K. Li, X. Luan, and D. Song, "Underwater image co-enhancement with correlation feature matching and joint learning," *IEEE Transactions on Circuits and Systems for Video Technology*, vol. 32, no. 3, pp. 1133–1147, 2022.

[23] S. Zhang, T. Wang, J. Dong, and H. Yu, "Underwater image enhancement via extended multi-scale retinex," *Neurocomputing*, vol. 245, pp. 1–9, 2017.

[24] C. Li, S. Anwar, J. Hou, R. Cong, C. Guo, and W. Ren, "Underwater image enhancement via medium transmission-guided multi-color space embedding," *IEEE Transactions on Image Processing*, vol. 30, pp. 4985–5000, 2021.

[25] G. Hou, N. Li, P. Zhuang, K. Li, H. Sun, and C. Li, "Non-uniform illumination underwater image restoration via illumination channel sparsity prior," *IEEE Transactions on Circuits and Systems for Video Technology*, 2023.

[26] L. Peng, C. Zhu, and L. Bian, "U-shape transformer for underwater image enhancement," *IEEE Transactions on Image Processing*, vol. 32, pp. 3066–3079, 2023.

[27] A. Naik, A. Swarnakar, and K. Mittal, "Shallow-uwnet: Compressed model for underwater image enhancement (student abstract)," in *Proceedings of the AAAI Conference on Artificial Intelligence*, vol. 35, no. 18, 2021, pp. 15 853–15 854.

[28] Q. Jiang, Y. Kang, Z. Wang, W. Ren, and C. Li, "Perception-driven deep underwater image enhancement without paired supervision," *IEEE Transactions on Multimedia*, vol. 26, pp. 4884–4897, 2024.

[29] Y. Kang, Q. Jiang, C. Li, W. Ren, H. Liu, and P. Wang, "A perception-aware decomposition and fusion framework for underwater image enhancement," *IEEE Transactions on Circuits and Systems for Video Technology*, vol. 33, no. 3, pp. 988–1002, 2023.

[30] X. Guo, Y. Li, and H. Ling, "Lime: Low-light image enhancement via illumination map estimation," *IEEE Transactions on Image Processing*, vol. 26, no. 2, pp. 982–993, 2017.

[31] S. Liu and Y. Zhang, "Detail-preserving underexposed image enhancement via optimal weighted multi-exposure fusion," *IEEE Transactions on Consumer Electronics*, vol. 65, no. 3, pp. 303–311, 2019.

[32] Q. Zhang, Y. Nie, L. Zhang, and C. Xiao, "Underexposed video enhancement via perception-driven progressive fusion," *IEEE Transactions on Visualization and Computer Graphics*, vol. 22, no. 6, pp. 1773–1785, 2016.

[33] M. Li, J. Liu, W. Yang, X. Sun, and Z. Guo, "Structure-revealing low-light image enhancement via robust retinex model," *IEEE Transactions on Image Processing*, vol. 27, no. 6, pp. 2828–2841, 2018.

[34] S. K. Dhara and D. Sen, "Exposedness-based noise-suppressing low-light image enhancement," *IEEE Transactions on Circuits and Systems for Video Technology*, vol. 32, no. 6, pp. 3438–3451, 2022.

[35] K. G. Lore, A. Akintayo, and S. Sarkar, "Llnet: A deep autoencoder approach to natural low-light image enhancement," *Pattern Recognition*, vol. 61, pp. 650–662, 2017.

[36] W. Ren, S. Liu, L. Ma, Q. Xu, X. Xu, X. Cao, J. Du, and M.-H. Yang, "Low-light image enhancement via a deep hybrid network," *IEEE Transactions on Image Processing*, vol. 28, no. 9, pp. 4364–4375, 2019.

[37] Y. Jiang, X. Gong, D. Liu, Y. Cheng, C. Fang, X. Shen, J. Yang, P. Zhou, and Z. Wang, "Enlightengan: Deep light enhancement without paired supervision," *IEEE Transactions on Image Processing*, vol. 30, pp. 2340–2349, 2021.

[38] B. Peng, X. Zhang, J. Lei, Z. Zhang, N. Ling, and Q. Huang, "Lve-s2d: Low-light video enhancement from static to dynamic," *IEEE Transactions on Circuits and Systems for Video Technology*, vol. 32, no. 12, pp. 8342–8352, 2022.

[39] C. Guo, C. Li, J. Guo, C. C. Loy, J. Hou, S. Kwong, and R. Cong, "Zero-reference deep curve estimation for low-light image enhancement," in *Proceedings of the IEEE/CVF Conference on Computer Vision and Pattern Recognition (CVPR)*, June 2020.

[40] F. Zhang, Y. Li, S. You, and Y. Fu, "Learning temporal consistency for low light video enhancement from single images," in *Proceedings of the IEEE/CVF Conference on Computer Vision and Pattern Recognition (CVPR)*, June 2021, pp. 4967–4976.

[41] Y. Jin, W. Yang, and R. T. Tan, "Unsupervised night image enhancement: When layer decomposition meets light-effects suppression," in *European Conference on Computer Vision*. Springer, 2022, pp. 404–421.

[42] R. Liu, L. Ma, T. Ma, X. Fan, and Z. Luo, "Learning with nested scene modeling and cooperative architecture search for low-light vision," *IEEE Transactions on Pattern Analysis and Machine Intelligence*, vol. 45, no. 5, pp. 5953–5969, 2022.

[43] Y.-H. Lin and Y.-C. Lu, "Low-light enhancement using a plug-and-play retinex model with shrinkage mapping for illumination estimation," *IEEE Transactions on Image Processing*, vol. 31, pp. 4897–4908, 2022.

[44] F. Lv, Y. Li, and F. Lu, "Attention guided low-light image enhancement with a large scale low-light simulation dataset," *International Journal of Computer Vision*, vol. 129, no. 7, pp. 2175–2193, 2021.

[45] R. Li, R. T. Tan, and L.-F. Cheong, "All in one bad weather removal using architectural search," in *Proceedings of the IEEE/CVF Conference on Computer Vision and Pattern Recognition (CVPR)*, June 2020.

[46] J. Pan, S. Liu, D. Sun, J. Zhang, Y. Liu, J. Ren, Z. Li, J. Tang, H. Lu, Y.-W. Tai *et al.*, "Learning dual convolutional neural networks for low-level vision," in *Proceedings of the IEEE conference on computer vision and pattern recognition*, 2018, pp. 3070–3079.

[47] Y. Zhang, Y. Tian, Y. Kong, B. Zhong, and Y. Fu, "Residual dense network for image restoration," *IEEE Transactions on Pattern Analysis and Machine Intelligence*, vol. 43, no. 7, pp. 2480–2495, 2021.

[48] S. W. Zamir, A. Arora, S. Khan, M. Hayat, F. S. Khan, M.-H. Yang, and L. Shao, "Multi-stage progressive image restoration," in *2021 IEEE/CVF Conference on Computer Vision and Pattern Recognition (CVPR)*, 2021, pp. 14 816–14 826.

[49] J. M. J. Valanarasu, R. Yasarla, and V. M. Patel, "Transweather: Transformer-based restoration of images degraded by adverse weather conditions," in *Proceedings of the IEEE/CVF Conference on Computer Vision and Pattern Recognition (CVPR)*, June 2022, pp. 2353–2363.

[50] J. Han, W. Li, P. Fang, C. Sun, J. Hong, M. A. Armin, L. Petersson, and H. Li, "Blind image decomposition," in *European Conference on Computer Vision (ECCV)*, 2022.

[51] H. Chen, Y. Wang, T. Guo, C. Xu, Y. Deng, Z. Liu, S. Ma, C. Xu, C. Xu, and W. Gao, "Pre-trained image processing transformer," in *Proceedings of the IEEE/CVF Conference on Computer Vision and Pattern Recognition (CVPR)*, June 2021, pp. 12 299–12 310.

[52] C. Wang, Z. Zheng, R. Quan, Y. Sun, and Y. Yang, "Context-aware pretraining for efficient blind image decomposition," in *2023 IEEE/CVF Conference on Computer Vision and Pattern Recognition (CVPR)*, 2023, pp. 18 186–18 195.

[53] B. Li, X. Liu, P. Hu, Z. Wu, J. Lv, and X. Peng, "All-in-one image restoration for unknown corruption," in *Proceedings of the IEEE/CVF*

Conference on Computer Vision and Pattern Recognition, 2022, pp. 17 452–17 462.

[54] Y. Si, X. Zhang, F. Yang, J. Wang, N. Cheng, and J. Xiao, "Aosr-net: All-in-one sandstorm removal network," in *2023 IEEE 35th International Conference on Tools with Artificial Intelligence (ICTAI)*. IEEE, 2023, pp. 641–645.

[55] W. T. Chen, Z. K. Huang, C. C. Tsai, H. H. Yang, J. J. Ding, and S. Y. Kuo, "Learning multiple adverse weather removal via two-stage knowledge learning and multi-contrastive regularization: Toward a unified model," in *Proceedings of the IEEE/CVF Conference on Computer Vision and Pattern Recognition (CVPR)*, June 2022, pp. 17 653–17 662.

[56] Z. Luo, F. K. Gustafsson, Z. Zhao, J. Sjölund, and T. B. Schön, "Controlling vision-language models for universal image restoration," *arXiv preprint arXiv:2310.01018*, 2023.

[57] N. Ahmed, T. Natarajan, and K. Rao, "Discrete cosine transform," *IEEE Transactions on Computers*, vol. C-23, no. 1, pp. 90–93, 1974.

[58] Q. Jiang, Z. Liu, S. Wang, F. Shao, and W. Lin, "Toward top-down just noticeable difference estimation of natural images," *IEEE Transactions on Image Processing*, vol. 31, pp. 3697–3712, 2022.

[59] C. O. Ancuti, C. Ancuti, R. Timofte, and C. D. Vleeschouwer, "I-haze: a dehazing benchmark with real hazy and haze-free indoor images," 2018.

[60] C. Li, C. Guo, W. Ren, R. Cong, J. Hou, S. Kwong, and D. Tao, "An underwater image enhancement benchmark dataset and beyond," *IEEE Transactions on Image Processing*, vol. 29, pp. 4376–4389, 2020.

[61] C. Wei, W. Wang, W. Yang, and J. Liu, "Deep retinex decomposition for low-light enhancement," *arXiv preprint arXiv:1808.04560*, 2018.

[62] X.-b. Kang, F. Zhao, G.-f. Lin, and Y.-j. Chen, "A novel hybrid of dct and svd in dwt domain for robust and invisible blind image watermarking with optimal embedding strength," *Multimedia Tools and Applications*, vol. 77, pp. 13 197–13 224, 2018.

[63] S. M. Pizer, E. P. Amburn, J. D. Austin, R. Cromartie, A. Geselowitz, T. Greer, B. ter Haar Romeny, J. B. Zimmerman, and K. Zuiderveld, "Adaptive histogram equalization and its variations," *Computer vision, graphics, and image processing*, vol. 39, no. 3, pp. 355–368, 1987.

[64] Z.-u. Rahman, D. J. Jobson, and G. A. Woodell, "Retinex processing for automatic image enhancement," *Journal of Electronic imaging*, vol. 13, no. 1, pp. 100–110, 2004.

[65] X. Guan, S. Jian, P. Hongda, Z. Zhiguo, and G. Haibin, "An image enhancement method based on gamma correction," in *2009 Second International Symposium on Computational Intelligence and Design*, vol. 1, 2009, pp. 60–63.

[66] K. Iqbal, M. Odetayo, A. James, R. A. Salam, and A. Z. H. Talib, "Enhancing the low quality images using unsupervised colour correction method," in *2010 IEEE International Conference on Systems, Man and Cybernetics*, 2010, pp. 1703–1709.

[67] B. Li, W. Ren, D. Fu, D. Tao, D. Feng, W. Zeng, and Z. Wang, "Benchmarking single-image dehazing and beyond," *IEEE Transactions on Image Processing*, vol. 28, no. 1, pp. 492–505, 2019.

[68] Z. Wang, A. Bovik, H. Sheikh, and E. Simoncelli, "Image quality assessment: from error visibility to structural similarity," *IEEE Transactions on Image Processing*, vol. 13, no. 4, pp. 600–612, 2004.

[69] C. O. Ancuti, C. Ancuti, R. Timofte, and C. De Vleeschouwer, "O-haze: A dehazing benchmark with real hazy and haze-free outdoor images," in *2018 IEEE/CVF Conference on Computer Vision and Pattern Recognition Workshops (CVPRW)*, 2018, pp. 867–8678.

[70] R. Zhang, P. Isola, A. A. Efros, E. Shechtman, and O. Wang, "The unreasonable effectiveness of deep features as a perceptual metric," in *2018 IEEE/CVF Conference on Computer Vision and Pattern Recognition*, 2018, pp. 586–595.

[71] L. K. Choi, J. You, and A. C. Bovik, "Referenceless prediction of perceptual fog density and perceptual image defogging," *IEEE Transactions on Image Processing*, vol. 24, no. 11, pp. 3888–3901, 2015.

[72] C. Ancuti, C. O. Ancuti, and C. De Vleeschouwer, "D-hazy: A dataset to evaluate quantitatively dehazing algorithms," in *2016 IEEE International Conference on Image Processing (ICIP)*, 2016, pp. 2226–2230.

[73] C. Fabbri, M. J. Islam, and J. Sattar, "Enhancing underwater imagery using generative adversarial networks," in *2018 IEEE International Conference on Robotics and Automation (ICRA)*, 2018, pp. 7159–7165.

[74] Q. Jiang, Y. Gu, C. Li, R. Cong, and F. Shao, "Underwater image enhancement quality evaluation: Benchmark dataset and objective metric," *IEEE Transactions on Circuits and Systems for Video Technology*, vol. 32, no. 9, pp. 5959–5974, 2022.

[75] K. Panetta, C. Gao, and S. Agaian, "Human-visual-system-inspired underwater image quality measures," *IEEE Journal of Oceanic Engineering*, vol. 41, no. 3, pp. 541–551, 2016.

[76] J. Yan, J. Li, and X. Fu, "No-reference quality assessment of contrast-distorted images using contrast enhancement," in *arXiv, 1904.08879*, 2019.

[77] W. Wang, C. Wei, W. Yang, and J. Liu, "Gladnet: Low-light enhancement network with global awareness," in *2018 13th IEEE International Conference on Automatic Face and Gesture Recognition (FG 2018)*, 2018, pp. 751–755.

Mingye Ju (Member, IEEE) received the bachelors degree in communications engineering and the Ph.D. degree in communications and information systems from the Nanjing University of Posts and Telecommunications, Nanjing, China, in 2010 and 2018, respectively. As a joint Ph.D candidate, he also received the Ph.D. degree in philosophy from the Global Big Data Technologies Centre (GBDTC), University of Technology Sydney, Sydney, Australia, in 2020. From 2019 to 2022, he was a Lecturer with the Nanjing University of Posts and Telecommunications and a Post-Doctoral Researcher with the Nanjing University of Science and Technology. He is currently an Associate Professor with the School of Internet of Things, Nanjing University of Posts and Telecommunications. He has published more than 30 peer-reviewed papers and conferences, including IEEE TIP, IEEE TCSVT, and IEEE TITS. He is also an Associate Editor of IEEE Signal Processing Letters and a Guest Editor of Electronics. His research interests include computer vision and image processing.

Chunming He received the B.S. degree in communication engineering from Nanjing University of Posts and Telecommunications, Nanjing, China, in 2021, and the M.E. degree in computer science from Tsinghua University, Beijing, China, in 2024. He is current a Ph.D. student with the Department of Biomedical Engineering, Duke University, Durham, USA. His research interests include computer vision and image processing.

Can Ding (Senior Member, IEEE) received the bachelors degree in integrated circuit and integrated system from Xidian University, Xian, China, in 2009, and the joint Ph.D. degree in electromagnetic fields and microwave technology from Xidian University and Macquarie University, Sydney, NSW, Australia, in 2016. From 2015 to 2017, he was a Post-Doctoral Research Fellow with the University of Technology Sydney (UTS), Sydney, where he is currently a Senior Lecturer with the School of Electrical and Data Engineering (SEDE), Faculty of Engineering and IT (FEIT), and also a Core Member of the Global Big Data Technologies Center (GBDTC). He is an IEEE AP-S Young Professional Ambassador in 2024. His contributions to the antenna and propagation society has been to advance the understanding and the evolution of cutting-edge technologies that are leading to the cost-efficient deployment of 5G networks. Notably, his works have facilitated the management and even elimination of self- and cross-band interference between the 3G/4G/5G antennas in base station systems. These pioneering research efforts have garnered recognition in the form of a prestigious ARC DECRA grant in 2020, Australias most prestigious grant for early career researchers. His state-of-the-art base station antenna works have occurred in close collaborations with industry and have been successfully translated into solutions for cellular network operators across Australia. His accomplishments encompass several research and industry projects, patented innovations, and a portfolio of over 100 publications in top-tier journals and conferences. Dr. Ding serves as an Associated Editor for IEEE ANTENNAS AND WIRELESS PROPAGATION LETTERS.

Wenqi Ren (Member, IEEE) received the Ph.D. degree from Tianjin University, Tianjin, China, in 2017. From 2015 to 2016, he was supported by the China Scholarship Council and working with Prof. Ming-Husan Yang as a Joint-Training Ph.D. Student with the Electrical Engineering and Computer Science Department, University of California at Merced. He is currently a Professor with the School of Cyber Science and Technology, Shenzhen Campus, Sun Yat-sen University, Shenzhen, China. His research interests include image processing and related high-level vision problems.

Lin Zhang (Senior Member, IEEE) received the B.Sc. and M.Sc. degrees from the Department of Computer Science and Engineering, Shanghai Jiao Tong University, Shanghai, China, in 2003 and 2006, respectively. He received the Ph.D. degree from the Department of Computing, The Hong Kong Polytechnic University, Hong Kong, in 2011. From March 2011 to August 2011, he was a Research Associate with the Department of Computing, The Hong Kong Polytechnic University. In Aug. 2011, he joined the School of Software Engineering, Tongji University, Shanghai, China, where he is currently a Full Professor. His current research interests include environment perception of intelligent vehicle, pattern recognition, computer vision, and perceptual image/video quality assessment. He serves as an Associate Editor for IEEE Robotics and Automation Letters, and Journal of Visual Communication and Image Representation. He was awarded as a Young Scholar of Changjiang Scholars Program, Ministry of Education, China.

Kai-Kuang Ma (Life Fellow, IEEE) received his Ph.D. degree in electrical and computer engineering from North Carolina State University, and Master of Science degree from Duke University, North Carolina, USA. His industrial working experience began with the IBM Corporation, USA (1984-1992), followed by serving as a Member of Technical Staff at the Institute of Microelectronics, Singapore (1992-1995). He began his academic career at the School of Electrical and Electronic Engineering, Nanyang Technological University, Singapore, as Lecturer, Senior Lecturer, Associate Professor (1995-2005) and Full Professor (2005-2023). He is currently with the College of Electronic and Information Engineering, Nanjing University of Aeronautics and Astronautics, Nanjing, China. His research interests are in the areas of digital image/video processing, computer vision, and machine learning and artificial intelligence. He was serving as the Singapore MPEG Chairman and the Head of Delegation (1997-2001). He had extensive editorship contributions in multiple top-tier IEEE journals, including IEEE Transactions on Image Processing (currently, Deputy Editor-in-Chief), IEEE Transactions on Circuits and Systems for Video Technology, IEEE Transactions on Multimedia, IEEE Transactions on Communications, and IEEE Signal Processing Letters. He is a Singapore Academy of Engineering (SAEng) Fellow, ASEAN Academy of Engineering and Technology (AAET) Foreign Fellow, AIIA Fellow, AAIA Fellow, and IEEE Life Fellow.